Annu. Rev. Earth Planet. Sci. 1994. 22:553–95

PHYSICS OF ZODIACAL DUST

Bo Å. S. Gustafson

Department of Astronomy, University of Florida, Gainesville, Florida 32611

KEY WORDS: meteoroids, radiation pressure, Poynting-Robertson drag, solar wind drag, Yarkovsky effect, Lorentz force, dust collisions, light scattering, thermal emission, dust temperature

INTRODUCTION

This review of the physics of zodiacal dust departs from earlier treatments in that it seeks to present a consistent framework to model the dust as nonspherical and inhomogeneous chondritic aggregates ranging from compact to highly porous structures. The objective is to address all aspects needed to model the optical, thermal, and dynamic properties of the zodiacal cloud. Because the use of nonspherical and/or aggregate dust models often is prohibitively cumbersome or solutions nonexistent, laboratory data and approximate solutions are used in comparisons with the spherical case.

A chronological model relating zodiacal dust to solar nebula dust and interstellar grains gives a theoretical basis for the chondritic aggregate model of interplanetary matter and provides a framework to relate specific models to their origin. There is direct evidence that a large fraction of the dust complex is of the chondritic aggregate kind. Relevant modeling parameters are based directly on observations and do not depend on the chronological model.

The zodiacal light is difficult to measure accurately from the ground due to air-glow contamination and a background of unresolved stellar objects. Observers usually report brightness averaged over several days, months, or years of observations. Space-based, optical observations are usually also averaged and presented in a compact form where fine structure and changes with the observer's vantage point are lost in the averaging process. However, extended sets of data on the infrared sky are now available. The

0084–6597/94/0515–0553$05.00

Infrared Astronomical Satellite (*IRAS*) mapped the infrared sky in great detail during its 1983 mission and zodiacal data from the *Cosmic Background Explorer* (*COBE*) will soon be available. The great detail of zodiacal features seen by *IRAS* and the changing perspective over the lifetime of the mission provide mission great impetus for analysis and modeling of the cloud.

Empirical models developed before *IRAS* of the spatial distribution of dust in the solar system were reviewed in a classic article by Giese et al (1986). These models are descriptive in nature and do not account for the laws of celestial mechanics. Dust orbital motion subject to non-gravitational forces give shape to real clouds (Gustafson et al 1987, Dermott et al 1992). Dynamical cloud models simulate the release of dust from a postulated source and use orbital mechanics to produce a spatial distribution at any specified epoch. Such models allow Dermott et al (1992, 1993a,b) to identify the asteroidal origin of the solar system dust bands, and likely contributions from six or more distinct Hirayama asteroid families. Contributions from several sources can be overlapped until the complex structure seen in data sets is reproduced, including seasonal variations and dependence on viewing direction. An understanding of the dust motion is the basis for this modeling. Dust dynamics is also the means by which source probabilities can be assigned to individual dust particles to be collected in Earth orbit.

Heliocentric orbits precess due to planetary perturbations. In the restricted three-body problem, orbits precess along the orbital plane of the massive bodies. The orbit of a "massless" test particle oscillates about a constant inclination as the line of nodes where the orbital planes intersect rotates. With more than 99.8% of the mass of the solar system concentrated in the Sun and 0.1% in Jupiter, the restricted three-body formulation gives a good qualitative approximation of orbital evolution in interplanetary space.

A cloud of particles develops rotational symmetry as orbits precess along Jupiter's orbital plane. This applies to interplanetary dust, comets, and asteroids, and is the basis for assuming rotational symmetry of the zodical dust cloud with the Sun at the center. Other planets have similar influence on interplanetary orbits. Each planet tends to precess orbits along its orbital plane. The resultant plane along which orbits precess depends on the distance to each perturbing planet. The planets also significantly displace the zodiacal cloud's axis of symmetry from the Sun. This can be seen in the *IRAS* data and is reproduced by modeling of particle dynamics (Dermott et al 1992, Xu et al 1993). This illustrates the need for dynamic cloud models.

Differential precession rates result from a finite spread over heliocentric distances and spreads the orbits of Hirayama asteroid families (created

from the breakup of larger asteroids) along resultant planes described above (hereafter called local precession planes). An imprint of the distribution of the Hirayama family asteroids is inherited by newly created dust particles as the family asteroids grind down in collisions with each other, background asteroids, and meteoroids. This stochastic production (see modeling by Durda et al 1992), forms a cloud with a spatial distribution that depends only on the fraction of nongravitational forces on the dust (Xu et al 1993). The spatial distribution evolves as dust particles lose orbital momentum and migrate toward the Sun. As the orbits continue to shrink, the local precession plane changes and orbits do not have time to fully spread out along the plane corresponding to a given heliocentric distance before the plane changes. This gives each cloud component, defined as particles with a given descent rate starting from a given source region, a specific and calculable shape. I therefore review the forces acting on zodiacal dust, and the optical and thermal dust properties necessary to this and other modeling efforts. Emphasis is on the underlying physics and on uncertainties involved in estimating the various physical processes on real particles. A model of zodiacal dust particle morphologies is a prerequisite.

DUST MODELS

While it is generally believed that some interplanetary dust particles contain nearly pristine material out of which the solar system formed, the meteoroid complex and the zodiacal cloud are not direct remnants of the presolar nebula. Nebula dust was stored in comets and asteroids, where it has been processed to varying degree before reemerging as part of a continuous size distribution of interplanetary objects. Sizes span from asteroids and cometary nuclei in the km range through meteoroids that are too small to be seen as individual objects, to dust particles that are seen collectively as they produce the zodiacal light through scattering of sunlight. A size range of 1 to 100 μm is usually implied by the word "dust."

Pristine Matter

A simple framework to model interplanetary matter and interpret observations emerges based on a simple chronology carried back to the formation of interstellar grains. Protosolar nebula dust is thought to consist primarily of ancient ice mantles condensed on silicate cores and evolved in interstellar space with a freshly condensed ice mantle from nebula gases (Greenberg 1988).

Silicate spheres grow by condensation in the outflow from cool super giant stars. Aggregates develop from dust-dust collisions. The existence of

interstellar polarization indicates that the classical grains responsible for most of the extinction at optical wavelengths are elongated and aligned. Aspect ratios of 1:2 to 1:3, i.e. 2 to 3 sphere arrays, agree with the degree of polarization; the wavelength dependence of extinction (interstellar reddening) is indicative of 10^{-1} μm sizes (Greenberg & Hage 1990). Some molecules condense and consolidate the structure through formation of an ice mantle. Billions of years of ultraviolet photoprocessing in interstellar space and cosmic-ray bombardment changes the ice into a refractory carbon-rich, oxygen-poor material. The grains are thought to evaporate and recondense from passing supernova shocks (Seab 1987); these might reemerge as a homogenized grain population by the time they become part of a star-forming nebula.

Temperatures in the protosolar nebula are thought to have ranged from over 1000 K near Mercury's orbit to the order of 50 K or less between Uranus and Neptune or beyond, where comets formed. Suess (1987) describes how matter in the innermost portions vaporize under these circumstances, allowing the elements contained locally in gas and dust to mix. Excess gas condenses on essentially pristine protosolar dust in the outer parts. Water ice with inclusions of 10^{-2} μm grains of polycyclic aromatic hydrocarbon (PAH) dominates in this outer mantle condensed in the solar nebula. Based on observed quantities and cosmic abundances, Greenberg & Hage (1990) adopted mass fractions in the outer parts of the nebula where comets form of 0.20, 0.19, 0.55, and 0.06 for the silicate, organic refractory, volatile ice, and PHA, respectively. The corresponding densities are 3.5, 1.8, 1.2, and 2 g cm^{-3}. This may be the pristine matter out of which comets and asteroids formed—the grandparents of today's meteoroids and zodiacal dust.

Chondritic Aggregates

The "Bird's-Nest" model of cometary dust originally proposed by Greenberg & Gustafson (1981) represents the dust as pieces of bulk cometary material of aggregated nebular dust from which water ice has sublimated. Assuming comet nuclei bulk densities of 0.6 g cm^{-3} (Sagdeev et al 1988, Rickman 1989), the mixture of solar nebula materials leads to a packing factor $p \approx 0.33$ in comets. The packing factor is defined as one minus the porosity or the fraction of volume occupied by material. In the absence of any compacting process, the depletion of volatiles leaves behind a $p \approx 0.15$ loosely packed tangle of refractory materials. The aggregation process was both computer simulated and mechanically simulated to build models used in analog light scattering measurements (Figure 1). These are updated versions of the original "Bird's-Nest" models of cometary dust. Each model consists of either 250 or 500 spheres with index of refraction

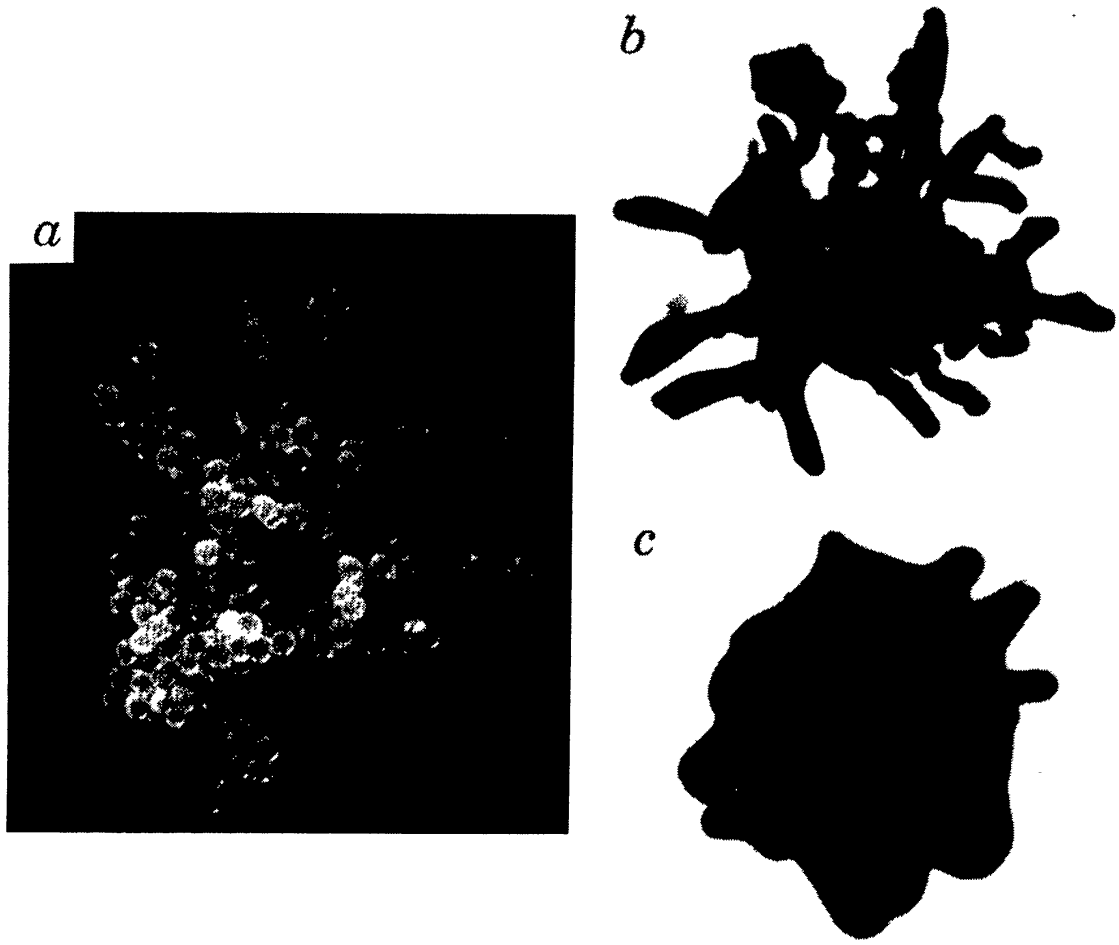

Figure 1 Examples of aggregate particle models used by Zerull et al (1993) and Gustafson et al (in preparation) in microwave analog light scattering measurements. (*a*) Each sphere represents a silicate grain grown by nucleation in the outflow from red giant stars. (*b*) The aggregates were coated by an absorbing compound to represent organic refractories grown in interstellar space. This is a chondritic aggregate of the "Bird's-Nest" type representing fresh comet dust. (*c*) Some aggregates were coated by a thicker mantle to represent a densely packed chondritic aggregate.

$n = 1.735 \pm 0.008 - 0.007\text{i} \pm 0.003\text{i}$ (Figure 1*a*). This material is representative of many silicates at visual wavelengths. The mantle coating the aggregate in Figure 1*b* has $n = 1.86 \pm 0.10 - 0.12\text{i} \pm 0.04\text{i}$ representing the organic refractory material. The model shown in Figure 1*c* has a thicker mantle of the same refractive index.

"Bird's-Nests" are aggregates of pristine interstellar grains that are characterized by a narrow size distribution. The aggregates derive from bulk material so that their dimension is three on the average—a whole number. These models are therefore not fractals (of fractal dimensions) despite their appearance. "Bird's-Nest" models represent the most pristine

solar nebula material that might be expected to reach Earth by natural means.

"Bird's-Nest" aggregates presumably originate from active areas exposing matter that has been protected in comet interiors. Refractory dust embedded in the porous ice matrix is released as exposed ice sublimates. Liberated dust particles are subject to gas drag and nuclear gravitation. Only pieces with sufficiently large effective surface-to-mass ratios are entrained by the gas. As dust particles with lower ratio accumulate on the surface, newly liberated dust is trapped in the interstices. A consolidated dust mantle of a structure and density largely dependent on the local gas flux can form nearly instantaneously (Shul'man 1972, Rickman et al 1990). The mantle obstructs gas flow and shields the ices from direct sunlight. Partial mantling of comet nuclei is now thought to be common and the coverage may vary over the orbit (Rickman et al 1990). New mantles build following ejection of the old one as the perihelion decreases (Rickman et al 1991). Mantle replacement or changing mantle coverage produces meteoroids and dust of processed cometary matter as ejected mantle fragments. In the models by Rickman et al (1990), dust mantles prevail until the gas pressure at the bottom exceeds the weight of the mantle. Some dust layers were found to eject as soon as they form, i.e. the mantle is carried away by the gas flow as soon as the interstices clog up and the gas pressure rises. Large amounts of compacted comet material can conceivably be continuously ejected in this process. Large meteoroids produced in this way should be in the shape of thin flakes.

Asteroid material appears to range from nearly comet-like assemblages of ice and organics among the Trojan D-type asteroids and Hilda P-types near and beyond the outer edge of the main belt to less pristine C and S types inside the asteroid belt (Gradie et al 1989). It is generally believed that this gradation with heliocentric distance reflects primordial properties of the solar nebula, with incomplete condensation of low-temperature ices in the main asteroid belt. About two thirds of the C-type asteroids appear hydrated, suggesting that water melted and soaked their minerals. This is seen in many carbonaceous meteorites, carbon-rich meteoroids that have survived atmospheric flight and are found on the Earth's surface. S-type asteroids may include assemblages of iron- and magnesium-bearing silicates mixed with metallic nickel-iron.

Dermott et al (1984, 1993b) find that the Themis and Koronis families produce the central solar system dust bands seen in the *IRAS* data and that the Eos family may be responsible for the 10° bands. Together, these families may produce as much as 10% of the zodiacal dust complex, with the whole asteroid belt producing 30% or more (Dermott et al 1993b). The Eos and the Koronis Hirayama families of asteroids have members

with spectra ranging from the S-type to intermediary between S and C. The Themis family contains C-type asteroids. Spectral similarities within families suggest that the parent bodies were not fully differentiated [see, for example, the article by Chapman et al (1989) for a review on asteroid families and Lipschutz et al (1989) for the relation between asteroids and meteorites]. Chondritic breccia material found in collisionally highly evolved meteorite materials with similar spectra are interpreted as representative of an extension to these Hirayama families. The breccias have essentially solar abundances of chemical elements. They are assemblies of chondrules, remnants of shocked interstellar grains that have been partially melted and depleted of volatiles. Repeated collisions compacted and partially fused the material into dense refractory assemblies. The compacted grains are typically a few micrometers across or less.

Given the average composition and high density of chondritic breccia (~ 3.5 g cm^{-3}), they may be modeled as a compact mixture of the same refractories as cometary dust. Average bulk densities of 2.1 ± 0.2 g cm^{-3} for S-type asteroids, given by Standish & Hellings (1989) as a preliminary value based on asteroid perturbation on the orbit of Mars, can allow for 15% by mass of water ice or a $p \approx 0.8$ packing. The average bulk density obtained for C-type asteroids, 1.7 ± 0.5 g cm^{-3}, leaves room for all the volatile ice in the primordial mixture or a packing factor as low as 0.7.

There is additional support for the general correctness of these Chondritic Aggregate models (hereafter CA-models) from chondritic interplanetary dust particles (IDPs) collected in the Earth's stratosphere. IDPs are separated from aerosols of terrestrial origin based primarily on their D/H isotopic anomaly. Most ($\sim 60\%$) of the collected IDPs are chondritic with approximately solar bulk composition of the rock-forming elements and are typically 5 to 50 μm across. Recent advances in sample preparation use ultramicrotomy to slice 3 to 10 μm thin sections of IDPs. Analytical electron microscopes (AEMs) allow the direct study of IDP morphology at resolutions approaching 0.01 μm (Bradley 1991). AEM studies confirm that chondritic IDPs can be divided into the olivine, pyroxene, and layer silicate groups proposed by Sanford & Walker (1985) based on infrared measurements, and show that all three classes of chondritic IDPs have an aggregate structure.

Pyroxene IDPs (Figure 2) are highly porous with a packing factor and overall structure approaching that of the "Bird's-Nest" model. However, the aggregate structure of rocky material prevails down to the resolution limit (Bradley 1991). Aggregation apparently took precedence over nucleation during their formation. If pyroxenes are unmodified "Bird's-Nests," then "classical" interstellar grains are aggregates. These could conceivably form in the turbulent wake of supernova shocks. Bradley

Figure 2 Electron micrograph of an ~80 nm thick section of a pyroxene-rich chondritic aggregate IDP collected in the stratosphere. Reproduced from Bradley (1991), by permission.

showed that only pyroxenes match the Fe to Mg distribution obtained by the PIA and PUMA mass spectrometers at Halley's comet. Analysis of IDP light elements including those in the CHON-particles discovered at Halley (Krueger et al 1991) remains elusive due to use of an epoxy organic polymer substrate to fix the fragile IDP material. The D/H ratio and existence of solar flare tracks show that the pyroxenes were not strongly heated during atmospheric entry. This is believed to be the most primitive class of collected IDP material.

Scanning Electron Microscope (SEM) analysis can distinguish two morphological types of chondritic dust (Flynn & Sutton 1990). Their characteristics are comparable to those inferred for our models. The densities are near 0.6 g cm^{-3}, presumably corresponding to pyroxenes, and 1.9 g cm^{-3}, which is close to the density of C- and S-class asteroids. However, only 15 low density particles and 10 of the higher density were analyzed and strong selection effects during collection could bias the data.

In addition, collected IDPs are a biased sample of the zodiacal dust

complex. Love & Brownlee (1991) found that spherical chondritic particles must be smaller than 50 μm in diameter to avoid melting even at 12 km s^{-1}, close to the lowest possible entry velocity at free fall (11.2 km s^{-1}). Most IDPs larger than 20 μm melt at entry velocities of 20 km s^{-1} and evaporate much of their initial material. Since the entry velocity of an average zodiacal particle is thought to be $\sim$30 km s^{-1}, most zodiacal dust particles disintegrate upon atmospheric entry. Samples retrieved from the stratosphere may be both orbit- and material-biased subsets of matter that intersects the Earth's orbit. It is usually assumed that IDPs are biased in favor of asteroidal dust because asteroids are typically on lower inclination, lower eccentricity orbits than comets, which leads to low entry velocities and in addition they may contain tougher material.

Other dust properties may also be biased. Using *IRAS* data, Dermott et al (1993c) found evidence for a configuration of dust trapped in outer resonance with the Earth as suggested from numerical integrations (Gustafson & Misconi 1986). Dust in low eccentricity and inclination orbits is preferentially trapped in these resonances and eventually breaks out of resonance following a close approach to the Earth. Dermott et al suggest that a substantial amount of dust enters the Earth's atmosphere as it breaks away from the resonance and may be a source of low-velocity particles of primarily asteroidal origin. The residence time in the resonances might explain long cosmic-ray exposure age of IDPs and meteorites (Thiel et al 1991) if these ages are confirmed. Major collisions throw particles out of resonance. Only particles that by chance avoid major collisions, and thus have long exposure ages, make it to the close Earth passage with increased probability of becoming IDPs and meteorites.

While the shape of collected chondritic IDPs is complex, they usually are equidimensional although there is some evidence for a shorter dimension, i.e. IDPs may rest flat on the filter (G. J. Flynn, private communication). Particles with elongation ratios greater than 4 would create elongated craters on lunar rocks according to Ashworth (1978), but such craters are not seen in large numbers. In conclusion, dust and most meteoroids are roughly equidimensional with the only exception being the hypothesized evolved comet-mantle meteoroids. Most zodiacal dust has an aggregate structure. The packing varies from $p \approx 0.1$ for comet dust ejected from free-sublimating regions to $p \approx 1$ for compact asteroid chondritic matter. Intermediary packing is expected for some asteroidal matter and comet ejecta from low activity regions. All have approximately solar composition. Although stony and nickel-iron IDPs account for approximately one third of all collected IDPs, this morphology probably corresponds to a smaller fraction of the total asteroid dust population and an even smaller fraction

of the total zodiacal dust population. Dust particles and meteroids are usually not homogeneous and spherical.

FORCES

Equations describing motion under solar gravity and planetary perturbations are found in standard celestial mechanics textbooks (i.e. Moulton 1970). Forces due to sunlight or the solar wind also are important on meteoroids and dust particles. Let a linear dimension s define the size of an arbitrary particle. While gravity is proportional to the volume (s^3), pressure forces are in most cases proportional to the surface (s^2), and electromagnetic Lorentz forces to s.

The primary force in each category—solar gravity, sunlight radiation pressure force, and the electric component of the Lorentz force—all are approximately equal on a 10^{-1} μm particle at 1 AU. Second-order gravity and pressure forces—planetary perturbations and Poynting-Robertson light drag—are comparable on particles in the 10^1 to 10^2 μm size range. Both must be accounted for in interpretations of the shape, orientation, and extent of the zodiacal cloud (Gustafson & Misconi 1986, Dermott et al 1992). Only the Lorentz force can usually be safely ignored on micrometer sized or larger zodiacal particles, except outside Jupiter's orbit where any zodiacal light is weak and particle number densities are low.

Solar gravitational attraction dominates on interplanetary particles with dimensions larger than ~ 1 μm. It is often practical to treat other forces as perturbations on the central force field from a solar point mass M acting on the point mass m at heliocentric distance r,

$$\mathbf{F}_g = -\frac{GMm}{r^2}\hat{\mathbf{r}}, \tag{1}$$

where G is the gravitational constant and $\hat{\mathbf{r}}$ the unit heliocentric radius vector.

Radiation Forces

The force due to sunlight radiation pressure is usually the second strongest. Insolation on a stationary surface area, g, perpendicular to the solar direction produces the force

$$\mathbf{F}_r = \frac{S_o g Q_{pr}}{r^2 c}\hat{\mathbf{r}}, \tag{2}$$

where S_o is the solar constant or radiation flux density at unit distance, c is the velocity of light, and Q_{pr} is the efficiency factor for radiation pressure

(van de Hulst 1957) weighted by the solar spectrum. Radiation pressure varies with heliocentric distance as the flux density of sunlight, which has an inverse-square dependence.

Because the gravitational attraction to the sun also has an inverse-square dependance on the heliocentric distance, it is customary to eliminate r by introducing the dimensionless quantity

$$\beta = -\frac{F_r}{F_g} = \frac{(S_o/r^2)(Q_{pr}/c)}{GM/r^2} \cdot \frac{g}{m} = C_r Q_{pr}(g/m), \tag{3}$$

where $C_r = 7.6 \times 10^{-5}$ g cm^{-2}. When the geometric cross-section-to-mass ratio of a density ρ (g cm^{-3}) and radius s (cm) sphere, $g/m = 3/4s\rho$, is substituted in Equation (3), it is equivalent to the expression given by Burns et al (1979).

The sun radiates nearly all of its energy in a narrow wave band around 0.6 μm so that the transition from geometric optics to Rayleigh scattering takes place in the micrometer size range. The efficiency Q_{pr} is usually calculated from Mie theory for homogeneous spheres (van de Hulst 1957). Figure 3 compares the resulting β with values for CA-structures. The solid

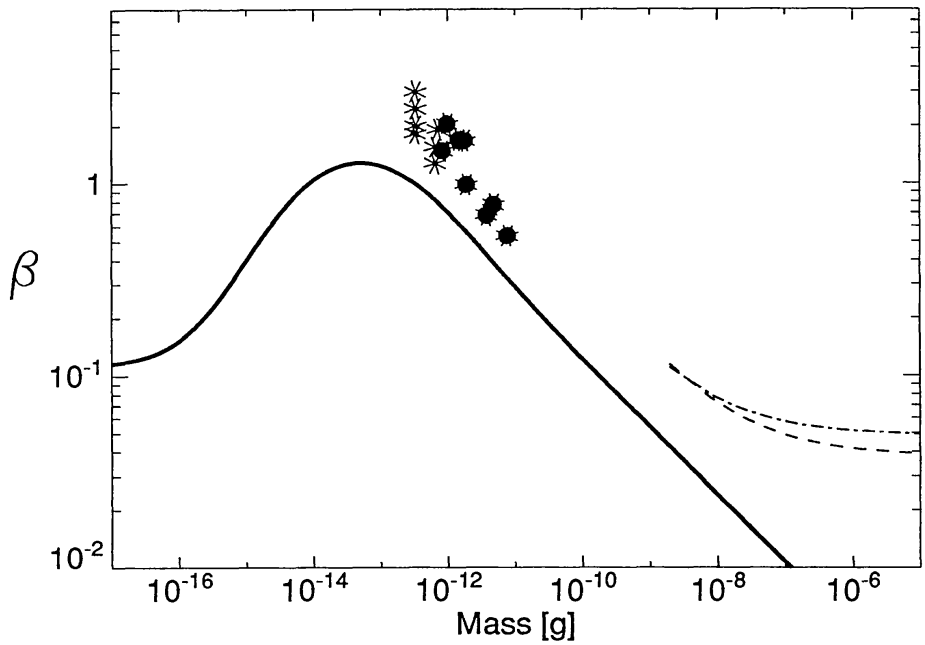

Figure 3 Ratio of radiation pressure force to gravitational force (β) as a function of particle mass. Mie calculations for homogeneous spheres (*solid curve*) consistently underestimates β values for aggregated dust models by a factor 2. Open symbols are for microwave analog measurements using aggregates of the type shown in Figure 1*a* and solid symbols are for those in Figure 1*b* and 1*c*. The dashed curve is for 10 μm thick flakes averaged over random orientation; dash-dot curve represents averages over the most likely spin orientation.

line shows the dependence of β on the mass of spheres using a bulk density $\rho = 2.5$ g cm^{-3} and optical constants for interstellar grain materials as given by Draine & Lee (1984) for their "astronomical silicates." The radiation pressure force is proportional to the geometric cross section at the large particle limit where geometric optics apply. The $\beta \propto s^{-1}$ slope shows that this is a good approximation for spheres above radius $s \approx 10$ μm, corresponding to $m \approx 10^{-11}$ g in the figure. The radiation pressure enhancement in the resonance scattering region below 10^{-11} g is discernible but not prominent in the log-log plot. The curve peaks in the 10^{-14} to 10^{-13} g or micrometer size range where the radiation force exceeds gravity on this particular material and thus the resultant force field is repelling. While β initially drops sharply at smaller sizes, β for natural materials never plummets as it does in some materials in plots by Burns et al (1979) where β for some materials appears to vanish. Instead, β must level off and approach a finite asymptotic value in the Rayleigh scattering region. This is because the efficiency for radiation pressure equals the efficiencies for absorption plus scattering: $Q_{pr} = Q_{abs} + Q_{sca}$. The scattering efficiency is proportional to s^4 and is responsible for the initial decrease. But natural materials have finite absorption and absorption is proportional to volume in Rayleigh scattering so that asymptotically $Q_{pr} = Q_{abs} \propto s$. This makes radiation pressure proportional to the volume (mass) so that β is independent of the size of small particles. The asymptotic dependencies

$$\begin{aligned} &\beta \propto g/m \qquad \text{at large } s \\ &\beta = \text{constant} \qquad \text{at small } s \end{aligned} \tag{4}$$

hold for all materials, particle shapes, and structures as long as only particle size s is varied.

Open symbols in Figure 3 are from microwave analog measurements (Gustafson et al, in preparation) using models like the one shown in Figure 1*a* adopting $\rho = 3.5$ g cm^{-3}. Solid symbols are for the same aggregates coated in a lossy mantle of density 1.8 g cm^{-3} representing an organic refractory compound (Figures 1*b*,*c*). The β values are approximately two times higher than for compact spheres of the same mass. The expected asymptotic behavior for large "Bird's-Nest" structures is that Q_{pr} is independent of size; β then varies as s^{-1} because the dimension is three and not fractal. The dashed curve in Figure 3 is for randomly oriented 10 μm thick cylindrical flakes representing the ejecta from low activity regions on comets. The smallest size corresponds to 10 μm diameter. Surface area-to-mass ratio and β decrease slowly with mass and β soon approaches the large size asymptotic value 0.039. The dash-dot curve is for the same flakes in the most likely nonrandom spin alignment: spin axis perpendicular to the

axis of symmetry and the solar direction (see the discussion on alignment below). The same material properties were used in the calculations for flakes as for the spheres. This illustrates that massive particles do not necessarily have small β values [see also the discussion of radiation pressure on nonspherical particles by Gustafson (1989)].

The β values for spherical shapes are the lowest as may be expected from the fact that g/m is at a minimum in this geometry. A widespread use of compact spherical models to represent interplanetary particles systematically underestimates β by a factor close to two, and more for large mantle-fragments. The only exception is at the smallest particle sizes (not shown) where the volume-integrated polarizability alone determines the radiation pressure force. In the Rayleigh scattering region $\beta \approx 0.11$ holds independently of the structure of particles made from "astronomical silicate" as long as the polarizability is isotropic.

Given the particle mass and β, the resulting force field acting on a stationary particle is

$$\mathbf{F} = -\frac{G(1-\beta)Mm}{r^2}\hat{\mathbf{r}}. \tag{5}$$

This can be equated to the gravitational field surrounding a mass $M(1-\beta)$ central star. A nonradial force component usually also is present on an arbitrarily oriented surface, but averages out on a sphere or any other body with rotational symmetry about $\hat{\mathbf{r}}$. In the section on particle spin, we see that random alignment is likely and that the preferred alignment also leads to vanishing nonradial components when averaged over the spin period, so that the form of Equation (5) remains valid.

In the unperturbed central force field, potential energy is constantly exchanged for kinetic energy, total energy and orbital momentum is conserved, and bodies can remain in solar orbit indefinitely. However, interaction with sunlight also generates a drag on moving bodies. Although the drag force is weak compared to the velocity-independent radial pressure force component, it dissipates energy and momentum thereby causing particles to eventually spiral into the Sun.

While there appears to be a consensus about the form of the equation of motion under radiation forces when applied to spherical solar system dust particles, its derivation using a relativistic formulation and the interpretation of the low-order velocity terms in classical (nonrelativistic) physics are still debated (see Klačka 1992 for a recent contribution). The same equation can be used to describe the motion of CA models.

Poynting-Robertson drag is due to the orbital motion around the Sun at velocity v. Solar system orbital velocities remain small compared with

the velocity of light and Poynting-Robertson drag can be thought of as arising from an aberration of the sunlight as seen from the particle and a Doppler-shift induced change in momentum. To the first order in v/c, the radiation force acting on a spherical particle is

$$|F_g|\beta[(1-2\dot{r}/c)\hat{\mathbf{r}}-(r\dot{\Theta}/c)\hat{\mathbf{\Theta}}], \tag{6}$$

where the unit vector $\hat{\mathbf{\Theta}}$ is normal to $\hat{\mathbf{r}}$ in the orbital plane (Burns et al 1979, Klačka 1992). The velocity-independent radial term representing force due to radiation pressure is given by Equation (2)—although not a pressure, it is often referred to simply as "radiation pressure." The second term along $\mathbf{r}$ is due to Doppler shift. With the transverse last term, this velocity-dependent part of Equation (6) is the Poynting-Robertson (PR) drag. Doppler shift enters twice: once due to the rate at which energy is received and a second time due to the reradiated and scattered radiation. Because aberration and Doppler shift apply independently of the particle morphology, radiation forces acting on the CA-models also can be expressed through the same formula with the proper β. With the addition of any nonradial pressure terms, Equation (6) applies to arbitrary particles.

PR drag dissipates the orbital angular momentum and energy of meter-size particles and smaller in the inner solar system on time scales of the age of the solar system. A particle with $\beta < 1$ starting in a circular orbit at the heliocentric distance r (AU), which does not experience net transverse pressure terms, spirals into the Sun in $400\, r^2/\beta$ years. Particles with higher β values escape from the solar system.

Solar Wind Corpuscular Forces

Except for the efficiency factor Q_{pr}, Equation (6) does not depend on the wave nature of light and has also been derived in a corpuscular formulation (Klačka 1992). Corpuscular forces due to collision with solar wind protons are therefore analogous to radiation forces and can be represented by an equation of the same form

$$|F_g|\beta_{sw}[(1-2\dot{r}/v_{sw})\hat{\mathbf{r}}-(r\dot{\Theta}/v_{sw})\hat{\mathbf{\Theta}}], \tag{7}$$

where v_{sw} is the solar wind speed. The ratio of proton pressure to gravity is

$$\beta_{sw} = -\frac{F_{sw}}{F_g} = \frac{(M_{p,o}/r^2)(C_D/2)}{GM/r^2}\cdot\frac{g}{m} = C_p(g/m), \tag{8}$$

where C_D is the free molecular drag coefficient and $C_p \approx 3.6\times10^{-8}\,\mathrm{g\,cm^{-2}}$. The proton momentum flux density at 1 AU, $M_{p,o} \approx 2.15\times10^{-8}\,\mathrm{dyn\,cm^{-2}}$, is nearly the same under fast and slow solar wind conditions. It is one of

the most stable solar wind quantities when averaged over a solar rotation (Steinitz & Eyni 1980, Schwenn 1990). It also appears invariant up to 30° heliomagnetic latitudes (Bruno et al 1986), the largest latitudes at which data are available at the time of writing (*Ulysses* will extend these data to higher latitudes). Any heliocentric dependence of the solar wind speed to 1 AU and beyond is neglected in Equation (8) as the possibility of an accelerating flow remains to be settled (Schwenn 1990).

The free molecular flow drag coefficient C_D, due to protons of mass m_p in a Maxwellian velocity distribution of temperature T_p impinging on a sphere from which the fraction ε is specularly reflected, is

$$C_D = \frac{2S^2+1}{\pi^{1/2}S^3}e^{-S^2} + \frac{4S^4+4S^2-1}{2S^4}\mathrm{erf}(S) + \frac{2(1-\varepsilon)\pi^{1/2}}{3S}\left(\frac{T_d}{T_p}\right)^{1/2}\left(1+Y_p\frac{m_s}{m_p}\right), \quad (9)$$

where $S = [m_p/(2kT_p)]^{1/2}|u|$, k is Boltzmann's constant, and u the relative velocity. Equation (9) simplifies considerably as S ranges from approximately 10 under high speed solar wind conditions to 15 at low speed conditions when the plasma is cooler. In this range the error function $\mathrm{erf}(S) = 1$, the first term in Equation (9) is negligible, and the second term is close to 2. The third term includes the contribution from reemitted protons at an average energy given by the dust temperature T_d. The term $Y_p(m_s/m_p)$ was introduced by Mukai & Yamamoto (1982) to account for sputtering of molecules of mass m_s at the yield Y_p. No sputtering corresponds to $Y_p = 0$ and results in $C_d = 2$ when proton velocity dispersions are neglected. This corresponds to complete momentum transfer from all protons that hit the dust particle. At solar wind proton temperatures, this remains a good approximation for most zodiacal dust particles. Even at the high dust temperatures reached around 0.1 AU from the Sun, the efficiency grows by less than 1% when reflections are specular and 1.5% when diffuse. Sputtering of magnetite increases C_D by less than 2.5% while the effect is even smaller on obsidian. These figures are obtained by inserting the same material parameters as Mukai & Yamamoto (1982) in Equation (9). Although water ice leads to slightly higher values, we shall see that volatile ice is not an important dust material inside the asteroid belt where nearly all the zodiacal light is produced.

The pressure due to other solar wind ions can be similarly calculated, but their contribution is less important. Mukai & Yamamoto (1982) showed that the term due to sputtering by helium nuclei is an exception and can increase the effective C_D by 35% for magnetite and 5% for obsidian. It can be shown that randomly oriented particles of any convex shape have the same averge C_D as a sphere by realizing that the dis-

tribution of orientation of each surface element is the same as surface elements on a sphere when averaged over all orientations (van de Hulst 1957). Concave and aggregate particles also lead to C_D values close to 2 as multiple scattering leads to more complete transfer of momentum.

The ratio of proton to light pressure is $(C_p \cdot C_D)/(C_r \cdot Q_{pr}) \approx 3.6 \times 10^{-8}/7.6 \times 10^{-5} \approx 4.7 \times 10^{-4}$ (assuming $Q_{pr} = 1$ and $C_D = 2$), thus solar wind corpuscular pressure is negligible compared to sunlight radiation pressure. However, the drag ratio is a factor c/v_{sw} larger because of the greater aberration angle and Doppler shift for protons than for light. The largest variations in the proton drag are caused by the solar wind speed and its dependence on heliocentric latitude and solar distance, not C_D. Average values during conditions of slow wind (<400 km s^{-1}) measured from *Helios 1* and *2* and *IMP 7/8* (Schwenn 1990) give the ratios 0.41 (*Helios*) and 0.43 (*IMP*) decreasing to 0.21 (*Helios*) and 0.20 (*IMP*) in the fast wind (>600 km s^{-1}). Average values over the missions give 0.29 (*Helios*) and 0.30 (*IMP*). *IMP* made measurements at 1 AU while the *Helios* data are normalized to 1 AU. At 0.3 AU *Helios 1* data indicate a 10.5% slower wind speed and *Helios 2* wind speeds were slower by 4.4% indicating that the proton drag to PR drag ratio may increase close to the Sun. The dependence on the latitude angle Θ above the current sheet in 1974 and 1985 is given in Figure 4 based on the velocity dependence derived by Kojima & Kakinuma (1990) using interplanetary scintillation

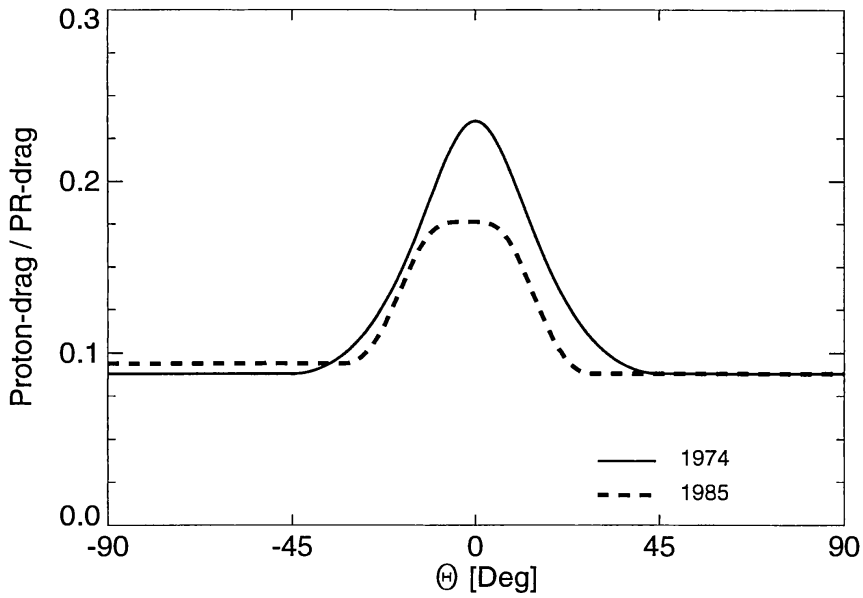

Figure 4 Solar wind proton drag in units of Poynting-Robertson drag in circular orbit plotted as a function of angular distance from the current sheet. The ratio is based on a constant proton momentum flux and interplanetary scintillation measurements (Kojima & Kakinuma 1990) of the solar wind speed in 1974 (*solid curve*) and 1985 (*dashed curve*).

data (IPS). High wind speed and low proton drag is typical at high latitudes.

Mukai & Yamamoto (1982) accounted for an expected net west flow of the solar wind based primarily on theoretical work by Weber & Davis (1967). Observers have been trying to detect this nonradial flow but the results are controversial and a radial flow remains a good approximation when averages are made over a solar rotation (Mariani & Neubauer 1990). The best estimates from *Helios* data is a 0.4° deviation—1/4 of the predicted value (Schwenn 1990). The resulting west pressure component is 0.7% of the radial proton pressure while proton drag is nominally of the order of 5% to 10% at 1 AU. The west pressure force is smaller than the uncertainty in the drag and can usually be neglected.

Solar Wind Lorentz Force

Particles in interplanetary space are charged and therefore couple to the interplanetary magnetic field moving with the solar wind. Photo-emission of electrons from the absorption of solar ultraviolet radiation dominates under normal conditions over the sticking of solar wind electrons so that dust particles have a positive potential $U \approx 5$ V (Goertz 1989). This corresponds to a $Q = 4\pi\varepsilon_o Us$ charge on a spherical particle where $\varepsilon_o = 8.859 \times 10^{-12}$ C V m^{-1} is the permeability of vacuum. The interplanetary magnetic field exerts a force

$$\mathbf{F}_L = Q\mathbf{v} \times \mathbf{B} \tag{10}$$

on the charge, where the velocity $\mathbf{v}$ is relative to the field. It is customary to write Equation (10) in terms of components due to a particle's heliocentric velocity $\mathbf{v}_g$ and the solar wind velocity $\mathbf{v}_{sw}$;

$$\mathbf{F}_L = Q(\mathbf{v}_g \times \mathbf{B} + \mathbf{v}_{sw} \times \mathbf{B}). \tag{11}$$

The second term is independent of the particle motion and can be viewed as resulting from an induced electric field. Equation (11) is then equivalent to Lorentz's equation and the force is referred to as the Lorentz force. The electric component is proportional to the azimuthal component of the magnetic field and always acts along the latitude or $\hat{\boldsymbol{\Theta}}$-direction in Parker's (1958) model of the interplanetary magnetic field. The electric component dominates everywhere, except at the poles where the azimuthal magnetic field vanishes. It is noteworthy that the electrical term is independent of solar wind speed. The Archimedean spiral becomes steeper with increasing wind speed, which decreases the azimuthal magnetic field component and keeps $\mathbf{v}_{sw} \times \mathbf{B}$ constant (Gustafson & Misconi 1979); wind speed variations have negligible effects on the Lorentz force.

Parker (1958) based his model on an expanding solar corona where

the magnetic field from sources on the Sun is "frozen" into the radially expanding solar wind plasma and drawn into an Archimedean spiral as the Sun rotates. At $r_o = 1$ AU, the average radial and azimuthal magnetic field components are $B_{r,o} \approx B_{\Phi,o} \approx 3$ nT, while the normal component $B_\Theta \approx 0$. At the heliocentric distance r and latitude Θ from the solar equatorial plane, the fields $B_r = B_{r,o} r^{-2}$, $B_\Phi = B_{\Phi,o} \cos(\Phi) r^{-1}$, $B_\Theta = 0$, are obtained assuming a constant solar wind velocity. The $\hat{\Theta}$-component vanishes assuming radial expansion and a radial field at the source. Parker's model is a good approximation of the time-averaged observed magnetic field (Mariani & Neubauer 1990).

Over a solar rotation, both the radial and azimuthal components may partially or fully average out in the interplanetary magnetic field sector structure, depending on latitude and the phase of the solar cycle. In the "ballerina model" by Alfvén (1977), a current sheet separates plasma from either hemisphere carrying fields of opposite polarity. A warped or tilted current sheet rotating with the Sun allows plasma from alternating hemispheres to reach the solar equatorial plane. Around solar activity minima the current sheet is nearly flat and aligned with the equator. *Pioneer 11* detected almost no inward-directed field lines over a whole solar rotation as it reached 16° northern heliographic latitudes in early 1976 (Smith et al 1978). This configuration is followed by a phase around the solar maximum when the heliopolar magnetic field undergoes polarity reversal. According to Saito (1988) the current sheet may be pictured as passing the pole and flipping during the reversal so that field directions are reversed at the next solar minimum as observed. Between these phases, a pseudo-aligned phase occurs when the magnetic quadrupole component is 10 to 20% of the strength of the dipole component and the current sheet is highly warped. This is followed by the excursion phase in which the quadrupole component diminishes and the tilt of the current sheet is intermediate between the reversing phase and the aligned phase. In calculating the Lorentz force, a simplified model may be used to describe the magnetic field strength averaged over a solar rotation. In this approximation, the current sheet changes its tilt angle ε at a constant angular velocity of $(1/11)\,\pi$ per year so that the averaged field at latitude Θ is a fraction $2 \arcsin(\tan\Theta/\tan\varepsilon)/\pi$ of the unipolar field.

Because solar wind velocities are high compared to orbital velocities, particle motion relative to the magnetic field is always in the solar direction. Positively charged dust particles always accelerate north when the magnetic field is directed outward and south when it is inward because the magnetic field Archimedean spiral curves in the direction opposite the solar rotation. The dominant electric part in Equation (11) is proportional to B_Φ and therefore to r^{-1}. This can make the instantaneous Lorentz force

particularly important on small grains at large heliocentric distances. The electrical component controls the flow of sub-micrometer interstellar dust grains through the heliopause and modulates the penetration deep into the solar system as a function of the solar cycle (Gustafson & Misconi 1979, Grün et al 1993b). As the Lorentz force acts on charges, the particle morphology enters only in the charging process. Charge measurements on individual interplanetary dust particles attempted from *Helios* indicated either extremely low particle densities or surface potentials of the order of 100 V (Leinert & Grün 1990) although $\sim$10 V is often assumed. More work is needed to understand the charge on aggregate particles.

Forces on Rotating Bodies

An additional set of forces arises on rotating bodies but their magnitude and even direction is controversial because these depend on several material properties and the state of rotation. Controversy is compounded by a range of competing effects that can cause spin and lack of direct evidence of the spin state. Some periodic comet nuclei, however, exhibit significant nongravitational forces and are known to have spin. The magnitude of the resulting accelerations is a complex function of the perturbed body's properties (Marsden 1976, Rickman et al 1991). As volatiles sublimate creating the coma and tails, a reaction force results. The nucleus may gain or lose orbital energy depending on its state of rotation as the evening side is warmer and undergoes heavier sublimation than the morning side. The situation is complicated by mantling and the development of active and inactive areas (Rickman et al 1991). Volatile dust particles leaving a comet should be similarly affected but only for a short time as volatiles soon are exhausted and their "jet engines" run out of fuel. Volatiles on dust particles might cause significant random motion and destroy dynamical information on their origin. While sublimation can have a large momentary effect, it will not act for long on small particles. Consequences of this phenomenon remain unexplored in the context of dust and meteoroids.

A related effect is due to asymmetry of the much weaker reaction force from thermal emission and may have a larger effect on rotating meteoroids and dust particles in the long run. The Yarkovsky effect is due to a hot evening hemisphere radiating more thermal energy than the cooler morning side. Like the sublimation force, this effect is hard to estimate because of its dependence on a detailed thermal dust model. However, the force on a large homogeneous sphere can be estimated following Burns et al (1979) by assuming that all energy is deposited at the surface, neglecting heat conduction to the dark side, and averaging the temperature over each hemisphere. Burns et al assumed that this "large particle" approximation

applies whenever the surface layer in which the temperature varies by a factor e^{-1} is thinner than the particle radius s. The force decreases rapidly with decreasing size below this limit and is soon negligible.

In this approximation, the Yarkovsky force F_Y on a particle with heat capacity C and thermal conductivity K is

$$\frac{F_Y}{F_{PR}} = \frac{W}{\sqrt{K\rho C}} \cdot \frac{\sqrt{P}}{r} \sin(\xi) \tag{12}$$

when expressed in units of the Poynting-Robertson drag in circular orbit F_{PR}. The spin of period P is about an axis making the angle ξ to the solar direction and the coefficient W is 1.31×10^7 ergs AU $\sec^{-1}$ K^{-1} cm^{-2} (Burns et al 1979). Efficiencies for absorption, emission, and Q_{pr} averaged over all wavelengths were assumed to be unity. The possibility of $\xi \neq 90°$ was not considered by Burns et al so the factor sin ξ is missing in their formula. The component along the orbit pole is $F_Y \sin \zeta$ and that opposing PR drag $F_Y \cos \zeta$, where ζ is the spin axis angle to the orbit pole.

Figure 5 shows a range of possible values of F_Y/F_{PR} as a function of

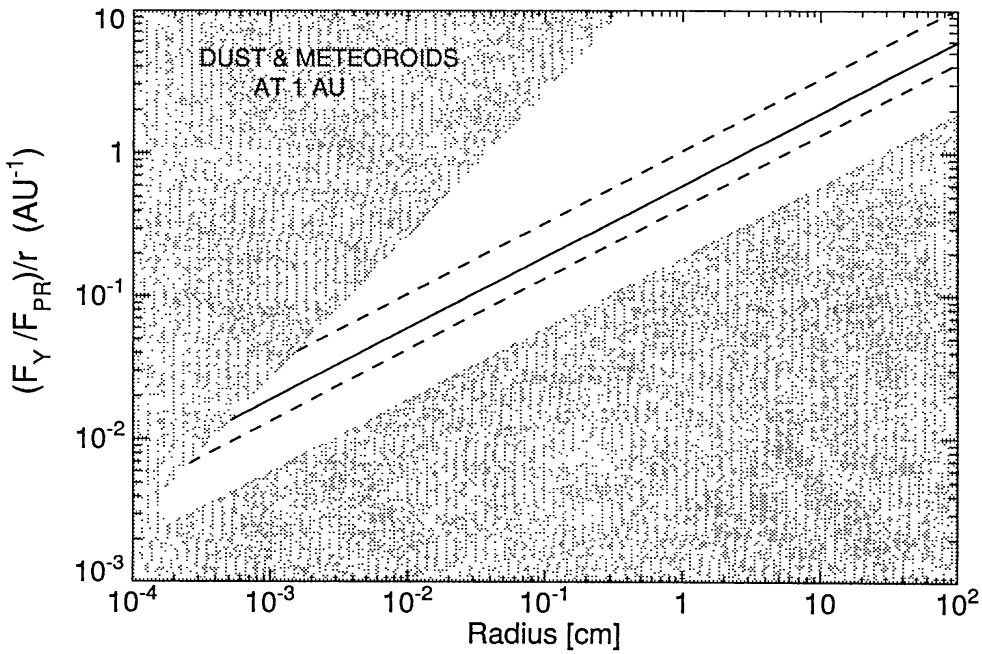

Figure 5 The Yarkovsky force to Poynting-Robertson drag ratio scales with heliocentric distance as r^{-1} and is given as a function of the radius of a spinning sphere. Collision experiments (Fujiwara 1987) gave average fragment spin rates that scale along the solid line. Dashed lines indicate the approximate range in spin rate. Thermal conductivity prevents particles from entering the shaded area to the left where the Yarkovsky force plummets in the diagram. Particles of a given spin rate are along horizontal lines and burst from internal stress before reaching the boundary to the shaded area on the right, which corresponds to the tensile strength of Basalt.

radius for a meteoroid or dust particle at $r = 1$ AU using $C = 10^{-7}$ ergs K^{-1} g^{-1}, $K = 3.5 \times 10^5$ ergs K^{-1} cm^{-1} sec^{-1}, and $\rho = 2.5$ g cm^{-3}. Since F_Y is proportional to the geometric cross section in this approximation as is F_{PR}, a given spin corresponds to a horizontal line in the figure. Thermal conductivity prevents particles from entering the shaded area in the upper left where the "large particle" approximation breaks down and the Yarkovsky force plummets. Centrifugal force-induced nonhydrostatic stresses vary with the size and spin as $\rho s^2(2\pi/P)^2$ (Weidenschilling 1981). Stony spheres cannot survive in the lower shaded area where stresses exceed the tensile strength of basalt (3×10^7 dyn cm^{-2}) (Fujiwara 1987) and particles burst. The incident radiation is attenuated by a factor e^{-1} at the depth $1/\gamma \approx 1.7$ μm, where $\gamma = 4\pi n'/\lambda$ is the absorption coefficient and the imaginary part of the refractive index $n' \approx 0.0294$ is for "astronomical silicate" (Draine & Lee 1984) at the wavelength $\lambda = 0.63$ μm where the solar spectrum peaks. The "large particle" approximation fails below $s \approx 1.7$ μm radius when solar radiation penetrates and deposits heat at a depth comparable to the particle size.

The region between dashed lines in Figure 5 corresponds to rotation periods for fragments from a basalt body. Fujiwara (1987) was able to record the rotation state of fragments produced in a central impact of a 0.37 g polycarbonate projectile on a 367 g basalt sphere at 2.5 km s^{-1}. These sizes correspond to fireballs although the experiment was primarily intended as a scale simulation of asteroid collisions and scales as shown by the lines (Fujiwara et al 1989). Experiments reported by Fujiwara et al also show that fragments have axial ratios near $2:\sqrt{2}:1$. Thus, given the approximations that went into Equation (12), they can be approximated by a sphere of the average radius.

The Yarkovsky force can be directed anywhere in the tangential plane depending on the spin orientation ζ. While the spin axis of fresh collision fragments has preferred alignments with respect to the impact direction (Fujiwara et al 1989), their spin alignment with respect to the orbital plane ζ is assumed to be random. This approximation may break down at high inclinations.

Competing mechanisms tend to align the spin axis of elongated particles. The solar wind tends to align the spin perpendicular to the sun-meteoroid direction, $\xi = 90°$. The condition of flow relative to a tenuous medium of impactors was also used by Gold (1952) in his discussion of the alignment of interstellar dust. Gold showed that prolate grains acquire spin as a result of randomly occurring collisions with gas molecules as the dust drifts through the interstellar gas. While the angular momentum produced by individual collisions can be in any direction, collisions producing angular momentum perpendicular to both the direction of gas flow and the

long axis are the most probable. In this process, Gold suggested that interstellar grains preferentially align their spin perpendicular to the gas flow direction and the long dimension. The same reasoning, if applied to impact fragments or to any prolate body, leads to a preferred spin axis perpendicular to the gas flow and the long axis or the axis of symmetry for oblate cylinders (flakes). Solar radiation forces have the same effect as the solar wind (Radzievskii 1952). While it is possible to conceive of particle geometries that tend to acquire spin alignment along the solar direction (Paddack & Rhee 1976), the radial direction changes continually forcing the particles to align on short time scales compared to the orbital period for the process to be effective. Only particles with a spin axis perpendicular to the orbital plane expose the same geometry all along the trajectory. The most probable systematic spin alignment of nonspherical particles is therefore perpendicular to the orbital plane.

The significance of this spin alignment is that the Yarkovsky force either adds to the Poynting-Robertson effect or counters it. Particles with spin parallel to the orbital momentum axis may remain in orbit while those with anti-parallel spin reach the Sun early. Under conditions where radiation-induced spin is significant, a spin axis could be stabilized by the temperature dependence of the albedo. This effect accelerates spin (Antyukh et al 1973) and maintains the axis orientation. Spin is balanced by rotational damping from a counterpart to the Poynting-Robertson drag (Jones 1990) so that a stable spin state may develop. Spin-aligned particles stay in orbit longer on the average, and elongated particles which acquire spin easily could accumulate in the cloud. However, this does not appear to be the case in the zodiacal cloud.

The degree of polarization from a cloud of randomly oriented particles vanishes in the back-scattering direction for symmetry reasons while small spin-aligned particles cause polarization. Polarization is not seen in the anti-solar, or gegenschein, direction (Weinberg 1985, Levasseur-Regourd et al 1991). Small aligned elongated particles evidently do not contribute a major portion of the zodiacal light. *COBE* measured linear polarization at around right angles to the Sun at 1.2, 2.2, and 3.5 μm. The 3.5 μm data are a particularly powerful indicator of spin-alignment (unless contaminated by scattering) as the neutral color of the zodiacal light suggests that the particles are not small and may be less effective polarizers at shorter wavelengths. Emission measurements can be in any direction and the polarization from a particle in the preferred alignment should be along its orbital plane. If no polarization is found, the likely reason is that the time scale for alignment is longer than the mean time between destructive collisions. Alternatively nondestructive collisions may randomize the spin.

Interestingly, either one precludes alignment of larger but otherwise similar particles by the same mechanisms. Like the Poynting-Robertson and solar wind drag times, the time scale for alignment is proportional to s, as it depends on the intercepted momentum per unit time and particle mass which is proportional to the cross section per unit mass. Probabilities for destructive collisions discussed below do not decrease fast enough with size to compensate for the longer time scale.

COLLISIONS

There are just a few dust particls per km^3 near the Earth's orbit. The particle number density decreases approximately inversely with the distance from the Sun and is even more tenuous away from the ecliptic plane. Collisions are not an important destruction mechanism for particles of micrometer size and smaller because their Poynting-Robertson lifetime is short compared to the mean time between catastrophic collisions. Collisions nevertheless greatly affect the evolution of large zodiacal dust particles and meteoroids. Experiments (Fujiwara et al 1989) confirm that at least in the size range of interest, the mass of the smallest impactor to cause a catastrophic collision is proportional to the target mass. The number of impactors N of mass greater than m is usually represented by a power law of the form $N(m) \propto m^{1-q}$ or $N(s) \propto s^{3-3q}$. The power-law representation is adopted for illustrative purposes; more complex size distributions develop under the combined effect of collisions and PR drag (Gustafson et al 1992). The mean time between catastrophic collisions $\tau_{CC}(s)$ is proportional to $N(s)$, while the Poynting-Robertson time $\tau_{PR}(s)$ at sufficiently large s is proportional to s. The ratio $(\tau_{CC}/\tau_{PR}) \propto s^{2-3q}$. Whenever $q > 2/3$, there is a transition to larger particles whose evolution is dominated by collisions rather than the Poynting-Robertson drag and radiation-induced spin. Most natural size distributions have much larger q values. Assuming that there are no external forces, particles collide and break up and eventually reach an equilibrium size distribution at $q = 11/6$, where newly produced fragments replace destroyed particles (Dohnanyi 1978). The transition to the collision-dominated regime is then quite sharp. This is illustrated in a numerical simulation using the empirical interplanetary particle flux derived by Grün et al (1985) to calculate the probability that a body in a 3 AU circular orbit in the ecliptic survives catastrophic collisions and reaches the Earth's orbit intact. Figure 6 shows that nearly all particles larger than 100 μm are destroyed and cannot reach Earth directly from the asteroid belt—unless they are perturbed into eccentric orbits by planetary perturbations (see Wetherill 1985).

Although Figure 6 shows that most 10 μm and smaller particles created

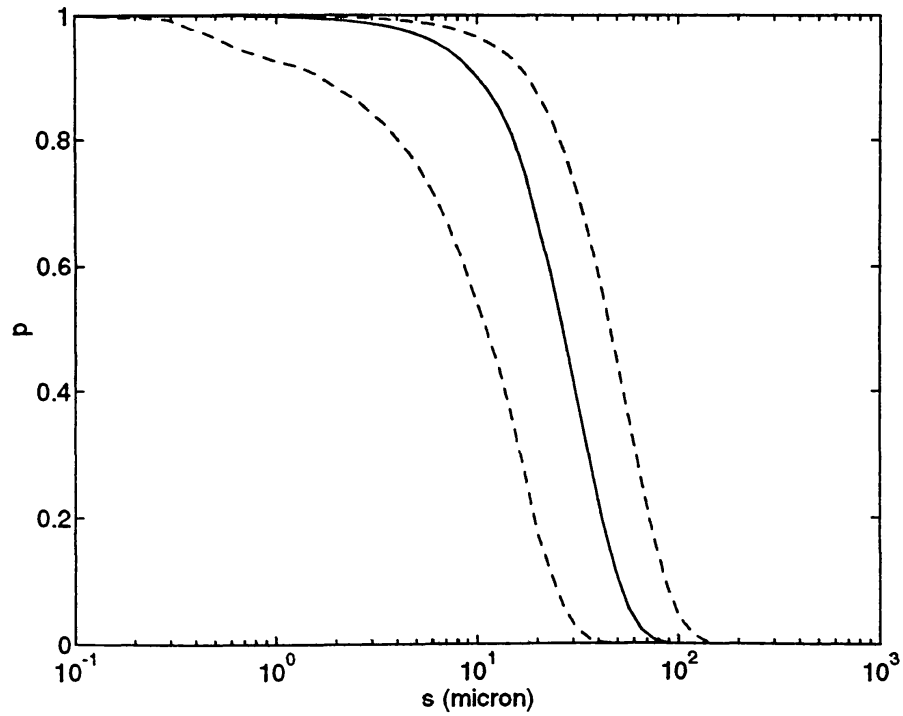

Figure 6 Probability (p) that a dust particle released on a circular orbit at 3 AU, and spiraling toward the Sun under Poynting-Robertson drag, survives catastrophic collisions and reaches the orbit of the Earth at 1 AU. Spheres of 2.5 g cm^{-3} density were exposed to a background of projectiles given by the empirical interplanetary particle flux (Grün et al 1985). Dashed curves indicate the estimated uncertainty.

in the asteroid belt reach the Earth intact, most particles in that size range are collision products from 100 μm or larger particles—unless waves of dust are produced in recent collisions such as modeled by Durda et al 1992. Practically all of the mass starts in the large particles; these break up creating a large amount of debris that also reaches the Earth as 10 μm or smaller fragments. The transition from PR-dominated particle sizes to the collision regime depends on the adopted catastrophic collision criterion, the impact strength, and the mean impact speed. Using reasonable assumptions of solar system conditions, the transition occurs within the 1 to 100 μm size range.

LIGHT SCATTERING

Observed optical properties of the zodiacal light are reviewed elsewhere (Weinberg & Sparrow 1978, Weinberg 1985, Leinert & Grün 1990, Levasseur-Regourd et al 1991). The implied optical properties of zod-

iacal dust, depending on the assumed particle distribution, are also discussed in these reviews, references therein, and by Lamy & Perrin (1991).

The derivation of an empirical angular scattering function for zodiacal dust from inversion of observed brightness and polarization requires knowledge of the particle number density distribution, although a few observing geometries (Levasseur-Regourd et al 1991) might be less sensitive to the assumptions. Levasseur-Regourd et al give evidence that dust properties vary with location but some general features are invariant: The scattering angle θ (180° − phase angle) dependence of the degree of linear polarization above $\theta \approx 70°$ is reminiscent of Rayleigh scattering except that the maximum polarization ($\theta \approx 90°$) is in the 20% to 30% range (or less depending on the distance from the Sun), as opposed to 100%. Another difference is the negative degree of polarization at $\theta > 170°$. This phenomenon is also observed in the scattering from many atmosphereless solar system bodies and in comets. Polarization vanishes at opposition as expected from particles in random orientation. An increased scattering intensity at large scattering angles—the opposition effect—is well established. The opposition effect cannot exclusively be due to a particle enhancement near the Earth, as the enhancement is also seen from deep space craft. Overall, the color of the zodiacal light normalized to the solar spectrum is neutral. The tendency over most of the optical range is toward the red and toward the blue below 2200 Å.

Modeling Angular Distribution

Giese (1973) found that key features of the zodiacal light can be fitted using Mie theory for spheres; this theory is still used by some investigators in the modeling of scattering by zodiacal dust particles. In many cases Mie theory is still the only practical way to integrate over particle sizes and wavelengths in the resonance region. The question addressed here is if Mie theory or any other (relatively) simple scattering theory can reproduce the scattering by CA-structures.

The aggregates shown in Figure 1 are used to test this hypothesis, although they probably are significantly smaller than the dust particles that produce most of the zodiacal light. Figure 3 shows that these models have high β-values and would leave the solar system on hyperbolic trajectories, if released from a large parent in circular orbit. A laboratory is under construction at the University of Florida to simulate and measure the scattering by larger aggregates.

Figure 7*a* shows the angular distribution of scattered optical light intensity (brightness) from an aggregate of 250 silicate spheres (Figure 1*a*) from microwave analog measurements averaged over azimuth rotation (Zerull et al 1993). Also shown are scattering functions based on some simple

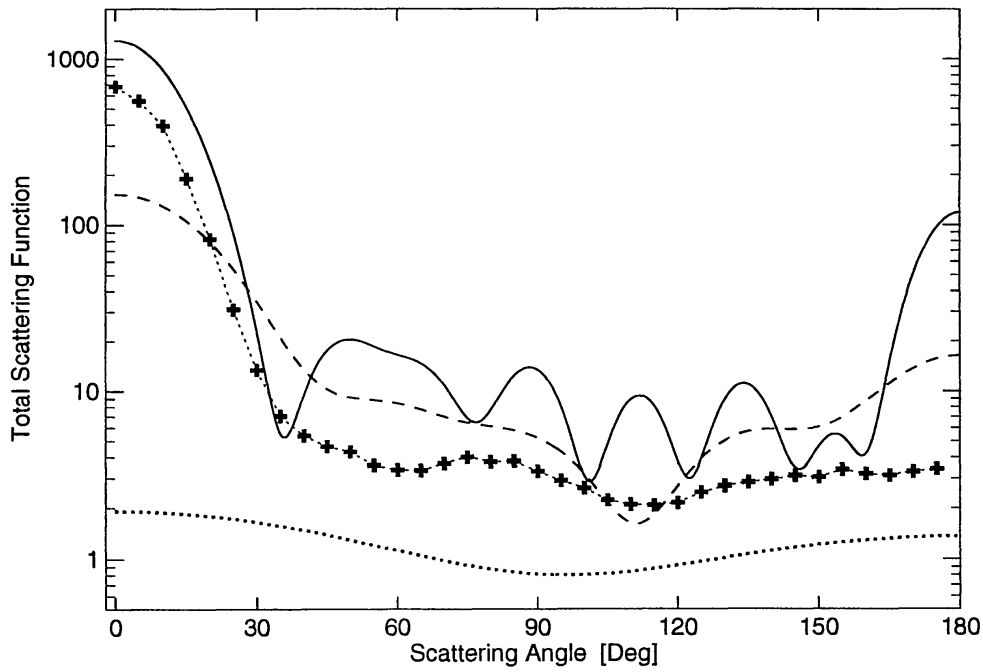

Figure 7 (*a*) Measured angular dependence of total scattered intensity from a 250-sphere aggregate without a mantle (*crosses*) and averaged over azimuthal rotation about three axes (from Zerull et al 1993). (*Solid curve*) Scattering by a sphere of the same material with a geometric cross section equal to the average cross section of the aggregate. (*Dashed curve*) Scattering by a sphere of volume equal to that of all the material in the aggregate. Independent and incoherent scattering by "unit" spheres is given by the dotted curve. None of these curves satisfactorily reproduces the measurements.

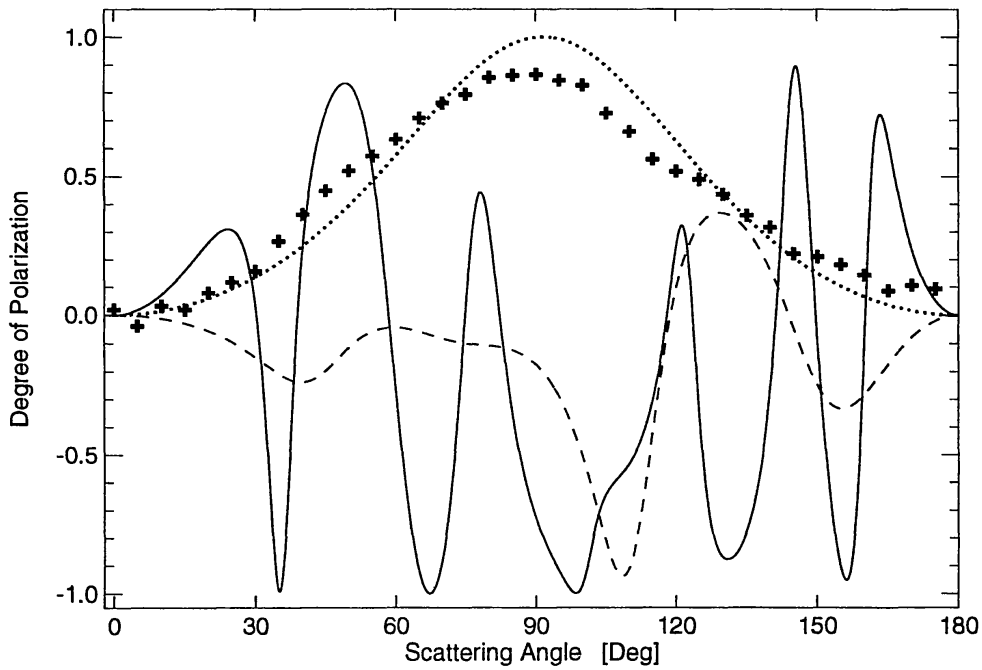

Figure 7 (*b*) Measured degree of linear polarization of radiation scattered from the 250-sphere aggregate as a function of scattering angle (*crosses*) averaged over all available orientations (rotation about three axes) from Zerull et al (1993). The polarization by independent "unit" spheres (*dotted curve*) is a good approximation at all angles, supporting the coherent scattering interpretation. The calculated polarization from both the equal cross section sphere (*solid curve*) and the equal volume sphere (*dashed curve*) are poor approximations.

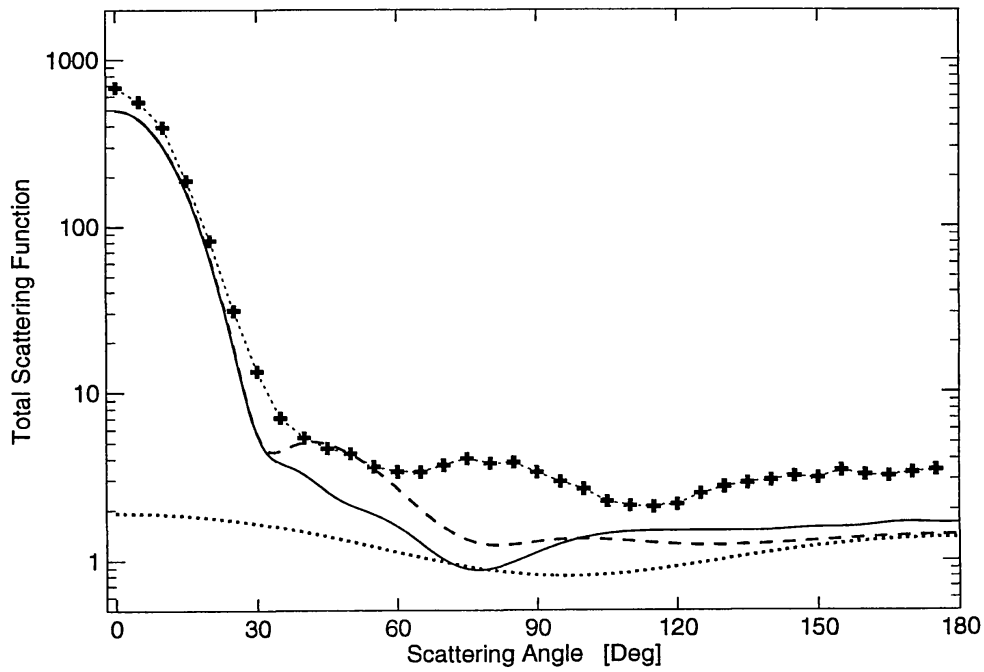

Figure 7 (*c*) Coherent scattering reproduces the measured scattering from the 250-sphere aggregate (*crosses*) better than any of the other approximations. Coherent scattering was computed from a computer reconstruction of the coordinates of each sphere within the aggregate from photographs. Coordinates were obtained for 249 of the 250 particles. (*Solid curve*) Average over rotation about the same axis of rotation as the measurements. (*Dashed curve*) Average over random orientations. (*Dotted curve*) Incoherent scattering. Reproduced from Zerull et al (1993).

model calculations. The dotted curve is for independent scattering—as the 250 spheres scatter light when dispersed in a tenuous cloud, their scattering adds incoherently at random phase. The dashed curve is for a single compact sphere in which all the material is consolidated. Its volume is the same as the compound volume of the 250 spheres in the aggregate without interstices or pores. The solid curve is for a larger sphere with geometric cross section equal to the average cross section of the aggregate. Both comparison spheres have the same index of refraction ($n = 1.735 - 0.007i$) as the individual spheres making up the aggregate.

None of these Mie calculations are satisfactory approximations. However, the Rayleigh-like degree of polarization from independent scattering by "unit" spheres is close to the measured values (Figure 7*b*) while the other calculations fail to reproduce the measurements. The dotted curve also represents polarization in the "coherent scattering" approximation. As used in this article, "coherent scattering" closely follows the Rayleigh-Gans scattering formulation (van de Hulst 1957) but uses summations over discrete scattering centers instead of integrals over a con-

tinuous medium. The phase shift suffered by contributions from different parts of the aggregate depends on the optical path length, which is assumed to be independent of the direction of polarization. The coherent scattering solution (solid curve in Figure 7*c*) is also the best approximation to the scattered intensity. Light contributed from all parts of the aggregate is in phase at $\theta = 0$ (forward scattering) but phase differences increase with increasing scattering angle. Phase coherence creates the forward scattering peak by constructive interference. Partial coherence at other directions and coupling between the units in the aggregate lead to increased scattering intensity over the incoherent scattering from a dispersed cloud (dotted curve). The angular scattering can be divided into three zones. Zone I is the forward scattering peak before the first minimum, where constructive interference dominates. The angular extent of this zone reflects the overall dimensions of the aggregate. This zone usually precedes a set of oscillations in zone II that contain information about the detailed distribution of matter within the aggregate. Oscillations dampen at higher scattering angles as phases randomize and any information about the internal structure other than from the increase in scattering intensity due to coupling appears to be lost in zone III which extends to $\theta = 180°$. The zones systematically shift to smaller angles as aggregates grow larger.

The dashed curve is the coherent scattering approximation using an analytic expression to average over orientations and happens by chance to fall between the solid curve and the measurements over much of zone II. The difference between the solid and dashed curves illustrates that averages over one azimuthal rotation (rotation axis perpendicular to the scattering plane) are expected to deviate from averages taken over uniform distributions of orientation, used to simulate randomness. Deviations can be particularly large in zone II. The enhanced measured scattering over the coherent scattering in most directions can largely be explained in terms of coupling between spheres (dependent scattering). The measurements can be reproduced within their uncertainties using a version of the Purcell & Pennypacker (1973) coupled dipole method (Gustafson et al, in preparation).

The coherent scattering approximation works best for aggregates without a coating while an "equivalent spheres" approximation based on the geometric cross section of the aggregate and an average index of refraction works better for coated aggregates. The geometric cross section is obtained by digitizing a photograph using a black and white scanner and counting the number of exposed pixels. This is repeated at twelve orientations. In the "equivalent spheres" approximation, scattering at each orientation is approximated using a sphere of equal geometric cross section and of an index of refraction intended to simulate even distribution of the material

over the volume of the sphere (Bruggeman 1935). Any equal cross section sphere approximates the shape of the forward scattering cone where most of the scattered intensity is confined. With the use of an averaged index of refraction, the magnitude also comes close to measured values. The "equivalent spheres" approximation in Figure 8 is the averaged scattering by the set of twelve spheres corresponding to the orientations at which the geometric cross section is known. Zerull et al (1993) show that the approximation grossly underestimates scattering outside the diffraction cone (zone I) by the tenuous aggregates without a mantle.

The most striking effect of applying the $n \approx 1.86 - 0.12i$ absorbing coat is that coherent scattering using core-mantle Mie theory for individual scattering centers grossly overestimates the magnitude of the scattering while the set of "equivalent spheres" becomes a better approximation to the brightness (Figure 8). Mie theory for homogeneous spheres might be a decent approximation for the scattering by aggregate structures when applied with great care, but usually is not. Coherent scattering usually is a decent approximation for the angular scattering by tenuous CA, while the equivalent spheres approximation appears promising for use with compact aggregates.

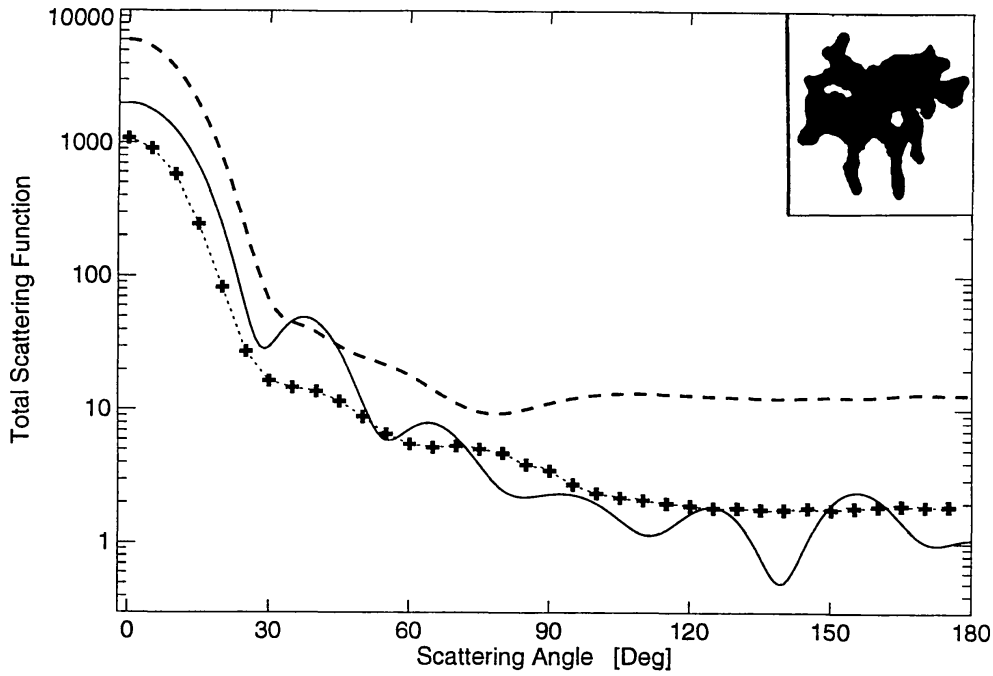

Figure 8 The measured total scattering function (brightness) for the 250-sphere aggregate (*insert*) coated by an absorbing mantle (*crosses*) compared to the "equivalent spheres" approximation (*solid curve*) and to coherent scattering (*dashed curve*). The set of "equivalent spheres" becomes a better approximation as a mantle is added.

Optical and Infrared Cross Section Efficiencies

The efficiency factor for scattering Q_{sca} is obtained by integration over the angular distribution discussed above. Particular care should be taken to fit the forward scattering cone, zone I, where most of the intensity is confined. The radiation pressure efficiency Q_{pr} was discussed in the section on radiation forces. The extinction efficiency is $Q_{ext} = Q_{sca} + Q_{abs}$, where the absorption efficiency Q_{abs} is discussed below.

The asymptotic solution for large spheres with finite absorptivity can be used to calculate $Q_{abs} = 1 - w$ for large convex particles in random orientation from the albedo w (van de Hulst 1957). That the solution for spheres is also valid for large randomly oriented objects of any concave shape is realized by considering that the sum of efficiencies for absorption and scattering by large spheres equals two. This is known as the extinction paradox (van de Hulst 1957). Half the energy goes into diffraction and in practice all refracted light is absorbed, i.e. any scattered light that is not diffracted comes from reflection and $Q_{abs} + Q_{ref} = 1$ where Q_{ref} is the efficiency for reflection. But, van de Hulst (1957, Section 8.42) showed that the scattering pattern caused by reflection from large, randomly oriented, convex particles is identical with the scattering pattern caused by reflection on a large sphere of the same material and surface condition. Logically, Q_{ref} is also the same for any other convex particle satisfying the same conditions. Therefore $Q_{abs} = 1 - Q_{ref}$ also is the same. In particular, Q_{abs} is the same for large randomly oriented plates, cylinders, ellipsoids, spheres, or any large convex particle of a given material.

Figure 9*a* illustrates the wavelength dependence of absorptivity Q_{abs} (=emissivity) for the interstellar grain material "astronomical silicate" (Draine & Lee 1984) at varying packing factors of concave randomly oriented objects at the asymptotic limit for large particle dimensions. Refractive indexes of the porous material were calculated assuming that matter is finely divided on scales of the wavelength so that the Maxwell-Garnett mixing rule applies. The condition is that the circumference to wavelength ratio of individual inclusions is much smaller than 1 (Maxwell Garnett 1904). This condition is fulfilled at infrared wavelengths when the inclusions are individual interstellar grains. To fulfill this condition at shorter wavelengths the inclusions have to be more finely divided, as expected in solar nebula processed matter. This is also a possible outcome of repeated collisions. The Q_{abs} values can be used to calculate the energy balance on concave bodies that are large compared with the longest wavelength at which they emit appreciable thermal energy. This condition requires particle dimensions larger than approximately $r^{1/2}$ centimeter, where r is in AU, but deviations from the dust temperature calculated

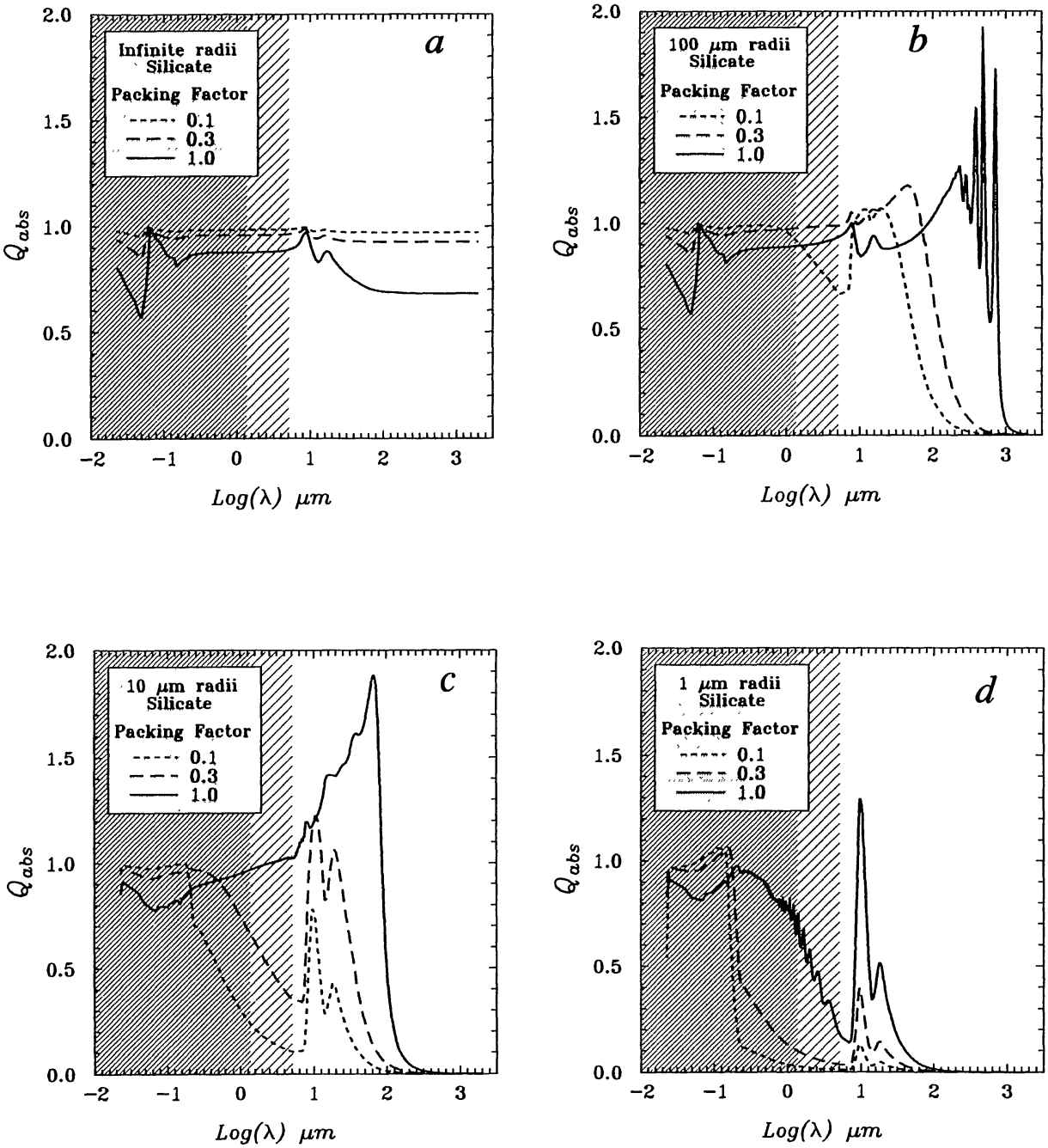

Figure 9 Absorption (and emission) efficiency $Q_{abs} = 1 - \text{albedo}$ for "astronomical silicate" by Draine & Lee (1984) as a function of wavelength at packing factors 0.1 (*dotted curve*), 0.3 (*dashed curve*), and 1.0 (*solid curve*). The Maxwell-Garnett mixing rule breaks down in the visual range (*shaded*) when unit grains making up the aggregate are $\sim 10^{-1}\mu$m (interstellar grain size) or larger. (*a*) Asymptotic solution for large particle radii. (*b*) For 100 μm radius spheres. The efficiency peaks in a highly structured spectrum beyond 100 μm for compact materials while the porous silicates have low efficiencies. (*c*) For 10 μm radius spheres. The 10 and 20 μm silicate features are seen in the porous materials. (*d*) For 1 μm radius. The silicate feature is seen at all packing factors.

using the asymptotic solution are negligible for particles as small as a tenth this size.

Absorptivity is nearly wavelength independent through the optical region ($\lambda = 0.4$ to 0.7 μm) where the Sun emits most of its energy though there are spectral features in the ultraviolet, and in the 1 to 100 μm region where most of the dust's thermal radiation is emitted. The well-known 10 and 20 μm silicate features are strongest in compact silicate. The drop in absorptivity at longer wavelengths practically disappears when the material is porous as more radiation penetrates inside the aggregate where it can be absorbed. Only a few percent escape absorption ($<4\%$) as opposed to over 10% for compact silicate at optical wavelengths and over 30% in the far infrared. Spectral features in the ultraviolet region of the spectrum have no practical importance to the energy balance.

For particle sizes in the resonance region, Q_{abs} is calculated using Mie theory. The absorptivity of 100 μm radii compact interstellar material shown in Figure 9*b* remains practically indistinguishable from the asymptotic solution through the ultraviolet, optical, and the infrared region down to about 10 μm but is dramatically enhanced at larger wavelengths. At the resonance absorption peak near 500 μm, the particles absorb over twice the energy falling upon them. This is impossible in geometric optics. The peak should best be seen in emission from 10 K or cooler particles that emit an appreciable fraction of their thermal radiation in that part of the spectrum. The resonance peak disappears completely for porous silicates for which that whole part of the spectrum is suppressed. A depression also develops in the 1–10 μm region at the lowest packing factor and the region around the 10 and 20 μm stands out as a broad feature. These features get sharper as the particle size decreases further. At 10 μm radius they become prominent as the absorptivity steadily decreases throughout the optical region until the silicate features are reached at 10 μm (Figure 9*c*). The absorptivity in the optical region for $p = 0.1$ aggregates is half that for a compact particle or of a 100 μm radius aggregate of the same packing factor. Compact silicates do not show distinctive silicate features until the particle size decreases further. Figure 9*d* shows the 10 and 20 μm peaks for a 1 μm radius particle, a sharp drop in absorptivity in the ultraviolet, and suppressed infrared peaks for porous grains.

TEMPERATURE

Reported zodiacal dust color temperatures near 1 AU are in the 255 K to 300 K range and decrease with heliocentric distance as $r^{-\nu}$ where $0.32 \lesssim \nu \lesssim 0.36$ (see the review by Hanner 1991 and references therein). Calibration problems with the *IRAS* data make the higher temperature

values more likely but we also should keep in mind that these color temperatures are based on emission near the 10 and 20 μm silicate features and could be significantly different from the actual grain temperature. The heliocentric gradient is less sensitive to calibration errors but is subject to uncertainties from the inversion process. If the gradient v really is significantly flatter than the expected 0.5 for large particles and flatter than 0.4 for small particles, this can be a significant constraint on the nature of the dust.

A large area-to-mass ratio allows dust particles and meteoroids to quickly reach their equilibrium temperature in interplanetary space so that the total energy gain equals the net loss. The energy balance of an isothermal body at heliocentric distance r with average cross section g presented to the Sun and total area G, is given by

$$\frac{1}{4\pi r^2} g \int_0^\infty L_\odot(\lambda) Q_{\text{abs}}(\lambda)\, d\lambda = G \int_0^\infty B(\lambda, T) Q_{\text{abs}}(\lambda)\, d\lambda + GH(T)Z(T), \quad (13)$$

where the left side represents the energy gain from sunlight of power $L_\odot(\lambda)$ at wavelength λ. The efficiency factor for absorption, $Q_{\text{abs}}(\lambda)$, is also the efficiency for emissitivity as a consequence of Kirchoff's law or time-reversal symmetry. The right side represents thermal emission across the Planck function $B(\lambda, T)$ at the dust particle temperature T and loss to sublimation, where $H(T)$ is the latent heat of evaporation and $Z(T)$ the sublimation flux.

Equation (13) is usually solved for the case of ideal black spheres with $Q_{\text{abs}} \equiv 1$, $G = 4g$, and $Z(T) = 0$. The resulting equilibrium "Black-Sphere" temperature in Kelvin at r AU is $T_{\text{B-S}} = 280\ r^{-1/2}$. It is often convenient to write the radiative equilibrium temperature of an arbitrary particle in terms of $T_{\text{B-S}}$ as

$$T = [(4g/G)(\langle Q_{\text{abs}} \rangle_{\text{opt}} / \langle Q_{\text{abs}} \rangle_{\text{ir}})]^{1/4} T_{\text{B-S}}, \quad (14)$$

where the average absorption efficiencies $\langle Q_{\text{abs}} \rangle_{\text{opt}}$ and $\langle Q_{\text{abs}} \rangle_{\text{ir}}$ are weighted by the Planck function $B(\lambda, T)$ at the solar color temperature and the dust temperature respectively, and $\langle Q_{\text{abs}} \rangle_{\text{ir}}$ is an average over all orientations.

Large Gray Particles

The equilibrium "Black-Sphere" temperature $T_{\text{B-S}}$ is a good approximation for a variety of particles larger than $\sim 10^4$ μm. It is seen directly in Equation (14) that the black-sphere radiative equilibrium temperature holds for spheres with the same absorption efficiency in the thermal infrared as in optical part of the spectrum. The condition of spherical shape is also

unnecessarily restrictive as the average geometric cross section of any convex particle with random orientation is precisely one quarter of the total area. This fact was rediscovered many times and a proof is given by van de Hulst (1957). This is particularly useful at large particle sizes where it was shown above that geometrical optics gives the same Q_{abs} for any convex particle of a given material when averaged over random orientations.

Temperatures of aligned convex particles also remain close to $T_{B\text{-}S}$. The ratio of the average area exposed to sunlight to the emitting area of a circular cylinder of radius s and length d spinning about the most probable axis is

$$\frac{g}{G} = \frac{2s^2 + 4sd/\pi}{2\pi s^2 + 2\pi sd}, \tag{15}$$

where the denominator comes from Equation (5) by Gustafson (1989). Large spinning flakes or plates that are ~ 10 μm thick (so that geometric optics applies) have a temperature excess over spheres of the same material of less than 6%. The equilibrium temperature of a thin flake $T_{B\text{-}S}(4g/G)^{1/4}$ is obtained using $\lim_{d\to 0}(g/G) = 1/\pi$. Thin needles are less than 5% cooler since $\lim_{s\to 0}(g/G) = 2/\pi^2$. Concave particles can be modeled similarly by adopting higher Q_{abs}-values to account for radiation trapping in cavities.

In conclusion, the radiative equilibrium temperature of a large black or gray particle at distance r (AU) is in the approximate range (Kelvin):

$$T_{B\text{-}B} = (280\, r^{-0.5})^{+6\%}_{-5\%}, \tag{16}$$

assuming that the particle is convex and of a material that has the same absorption efficiency in the infrared as in the optical part of the spectrum. The total radiated power is proportional to T^4 and G; the cylinder emits $g/\pi s^2 = 2/\pi + 4/\pi^2\, d/s$ times the power radiated by a sphere of radius s submerged in the same radiation field. This makes the radiative equilibrium temperature nearly independent of shape of randomly oriented large convex particles.

Small Gray Particles

Particles with dimensions 10^{-2} μm or less are in the Rayleigh region over practically the whole solar spectrum and also radiate their thermal energy as Rayleigh particles. In this limit, the absorption efficiency can be written $Q_{abs} = (8\pi^2/g\lambda)\,\mathrm{Re}(i\alpha)$. The polarizability α depends on the index of refraction n and the particle shape. As long as α is isotropic, it is independent of the distribution of matter within the tiny particle and proportional to the volume (van de Hulst 1957). Integration over the Planck function

and substitution into Equation (14) gives $T_{B\text{-}R} = (T_\odot/T_{B\text{-}R})^{1/4} T_{B\text{-}S}$, where $T_\odot = 5785$ K is the solar color temperature. The small size asymptotic temperature is then

$$T_{B\text{-}R} = 513 r^{-0.4}. \tag{17}$$

The slower temperature decrease with r is due to decreasing average emissivity efficiency as the particle cools. A black or gray Rayleigh particle is 233 K hotter than a large particle at 1 AU. In reality matter is not black or gray, most materials increase in absorptivity in the infrared, and small particles are sensitive to these variations. However, it is instructive to consider material and size effects separately.

Gray Particles of Arbitrary Size

The dust temperature strongly depends on the scattering regime that contributes most to the optical and infrared averaged absorption efficiencies. The dashed curve in Figure 10 illustrates the effect of changing the size of a sphere made of an ideal "gray" material ($n = 1.41 - 0.1i$). As

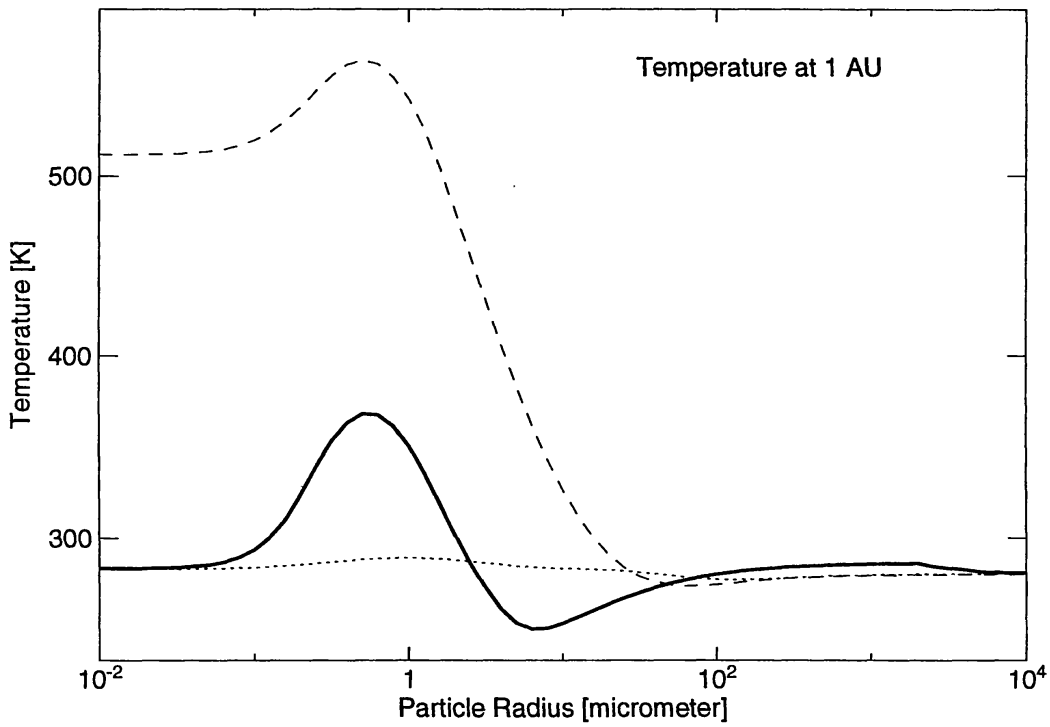

Figure 10 Radiative equilibrium temperature at 1 AU. (*Dashed curve*) Ideal "gray" material, $n = 1.41 - 0.1i$ at all wavelengths. (*Solid curve*) "Astronomical silicate" by Draine & Lee (1984). (*Dotted curve*) A $p = 0.1$ packing of the same material. The heliocentric temperature dependence ν is 0.5 for large particles and 0.4 for small sizes. The temperature difference between large and small particles of a given material is large at most heliocentric distances.

the size of the large sphere decreases, thermal emission enters the resonance region of increased emission causing the dust temperature to drop slightly. The temperature increases as the radius shrinks further and thermal emission enters the Rayleigh region. Peak temperature is reached when the solar spectrum is in the particle's resonance region. At smaller sizes, the solar spectrum also enters the Rayleigh region and the grain reaches its asymptotic Rayleigh temperature. Nonspherical particle shapes lead to qualitatively similar transitions. Equation (17) suggests that small particles in the solar system are always hotter than large particles of a similar material as the crossover point is inside the Sun at 0.5 solar radii. However, natural materials are not black and small particles are not always hotter than large ones of the same material.

Chondritic Aggregate Material

The solid curve in Figure 10 is for a compact sphere using the same material (by Draine & Lee) as used to generate Figure 9. The qualitative features from the ideal black material can be recognized but the net temperature increase towards small sizes is compensated for by increased material-dependent emission in the infrared (the 10 and 20 μm features); this compensates for the Rayleigh $Q_{abs} \propto \lambda^{-1}$ dependence and brings the asymptotic temperature back to $T_{B\text{-}S}$. While this qualitative behavior is common to many natural materials it is unusually strong in silicates because of the 10 and 20 μm emission features. The temperature dependence on heliocentric distance is still flatter than $r^{-0.5}$. The size dependence of an ideal "gray" material is approached at large heliocentric distances. The dotted curve is for $p = 0.1$ and the temperature of these porous structures of finely divided matter remains within 10 K of $T_{B\text{-}S}$. The temperature of "Bird's-Nest" structures is not represented by any of these curves as individual grains in the aggregate are not small compared to the optical wavelengths where most solar energy is emitted. If the aggregate is sufficiently porous, the absorption cross section in the visual range approaches that of the individual grains. However, the aggregate may act as an ensemble at the longer wavelength of thermal emission and porous particles enter the Rayleigh regime at larger dimensions than compact particles, thus the Rayleigh $\nu = 0.4$ heliocentric temperature dependence may apply. As the porosity increases, grains decouple and the temperature asymptotically approaches that of the individual constituent grains in free space. Figure 10 shows that if this model applies, compact zodiacal particles in the 1 to 100 μm interval should be cooler than $T_{B\text{-}S}$; sub-micrometer grains should be hotter. Individual or loosely aggregated grains of the size of interstellar grains and many grains found in chondrites are hot. Using similar calculations, Greenberg & Hage (1990) and Hage & Greenberg

(1990) showed that, if the emitting particles in comet Halley's coma can be represented by this kind of model, they must either be smaller than ~ 1 μm or porous with a packing less than $p = 0.2$ to fit the temperature and the emission features at 9.7 and 3.5 μm.

SUBLIMATION

Absorption of sunlight and thermal emission dominates the energy balance of most particles while sublimation can be a large heat sink on dust with volatile materials for a short time. Small particles rapidly run out of volatile coolant because of their high surface-to-volume ratio. The sublimation rate of water ice at temperature T is

$$Z(T) = \frac{b}{\sqrt{T}} e^{-H(T)/RT}, \tag{18}$$

where $b \approx 2 \times 10^{32}$ molecules cm^{-2} sec^{-1} K$^{1/2}$ or 6×10^{9} g cm^{-2} sec^{-1} K$^{1/2}$ of water and R is the gas constant. Division by the ice density $\rho = 0.92$ g cm^{-3} gives the surface recession rate. This rate is very temperature sensitive and pure water ice is nearly transparent at optical wavelengths, i.e. it is a notoriously poor absorber of sunlight while it radiates effectively in the infrared. The resulting temperature is low enough to make water ice meteoroids stable against sublimation throughout much of the outer solar system (Patashnik & Rupprecht 1975). But as little as 1% by volume of the "astronomical silicate" distributed in the ice brings the absorptivity close to unity and the radiative equilibrium temperature close to the black-body temperature. This phenomenon was also pointed out by Hanner (1981) and Lichtenegger & Kömle (1991). Figure 11 shows the estimated surface recession rate of water ice in a permeable isothermal mixture representing large fresh comet dust particles of the "Bird's-Nest" kind. The recession rate is tens of micrometers or more per year throughout the main asteroid belt. Sublimation becomes an efficient coolant inside 2.2 AU where the particle reaches 160 K, but is inconsequential further out.

If water ice fills the interstices in a centimeter-sized "Bird's-Nest" dust particle and sublimates at a controlled rate, a 1% temperature decrease could only be sustained for about a week at 1 AU. This is negligible compared with the dynamical life time. If the ice sublimates freely into vacuum the temperature drop is larger but the ice sublimates in seconds. Figure 12 shows the heliocentric distance where dust reaches 160 K using the same materials as in Figure 9. This is a conservative limit for the existence of water ice on dust particles. A large black sphere reaches $T_{B\text{-}S} =$ 160 K near 3 AU; this is also the asymptotic large size limit both for the

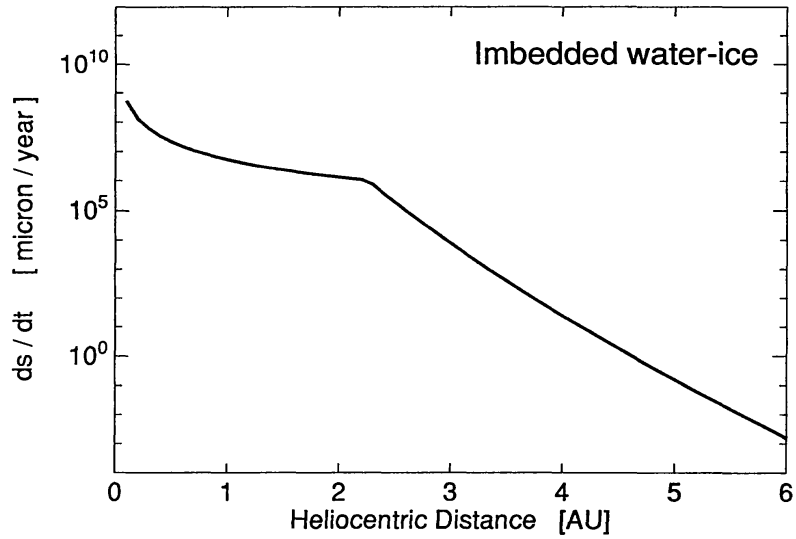

Figure 11 Surface recession rate for freely sublimating water ice imbedded in a large "Bird's-Nest" structure, as a function of heliocentric distance. The refractory materials increase the overall absorptivity so that most of the incident sunlight is absorbed. The equilibrium temperature is dominated by radiative equilibrium outside 2.2 AU where the sublimation rate is too slow to provide efficient cooling. Sublimation rapidly becomes an effective coolant inside this distance.

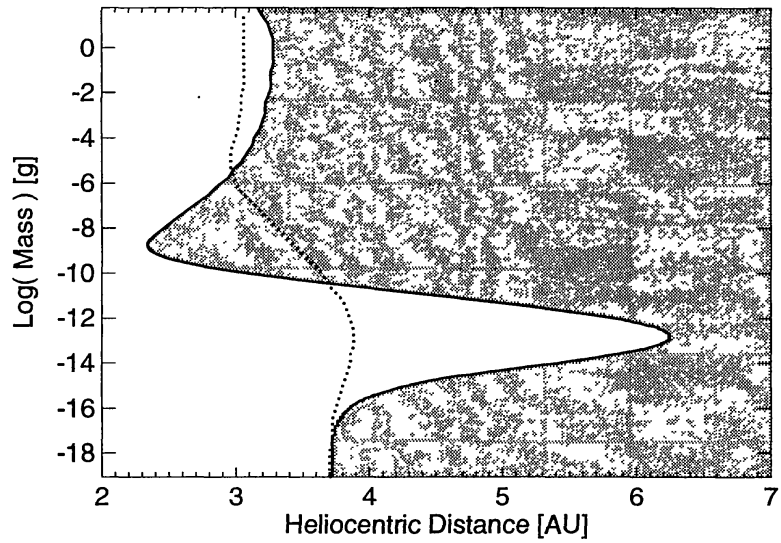

Figure 12 Isotherm of 160 K for dust particles in radiative thermal equilibrium. This is a conservative limit inside which water ice can not exist on dust particles. Interstellar dust grains in the 10^{-13} or 10^{-14}g range are efficient absorbers of sunlight and Rayleigh scatterers in emission so that they become substantially hotter than large particles and should lose their water ice near Jupiter. (*Solid curve*) "Astronomical silicate" by Draine & Lee (1984). (*Dashed curve*) Prous "astronomical silicate" with a packing factor of $p = 0.1$.

compact (*solid curve*) and the porous (*dotted*) models. The curves reflect the same phenomena seen in Figure 10 as thermal emission transits from the geometric optics region at large sizes to the Rayleigh region at the smallest sizes. The Rayleigh region isotherm is clearly shifted outside the large size ice limit due to the $v < 0.5$ heliocentric temperature dependence.

The optical constants used in the "compact material" calculations were derived from observed properties of interstellar grains (and inverted using Mie theory; Draine & Lee 1984). Interstellar grains with masses $\sim 5 \times 10^{-13}$ g were recently detected by *Ulysses* (Grün et al 1993). If the local interstellar grains are similar to the ones used to obtain the optical constants, any water ice should be lost near Jupiter's orbit where the grains were detected. Lower isotherms corresponding to more volatile materials have even greater size dependence.

CLOSING REMARKS

At a given wavelength, a dust particle intercepts an amount of energy that is proportional to $gQ_{\text{ext}}r^{-2}$. Each particle absorbs a fraction of this energy and emits it as thermal radiation in the infrared; the remaining energy is scattered and dispersed over scattering angles. This gives each dust particle a wide range of options to handle its energy budget. Large white particles scatter most of the intercepted light close to the original direction. If such particles are present, they would hardly be seen unless we look close to the Sun where observations are difficult. Smaller white particles scatter light over a wider angular range and observations away from the Sun are increasingly biased toward smaller particles. Around the polarization maximum near 70° from the Sun, large and intermediate size particles contribute most of the polarized brightness along the scattering plane where small particles cannot scatter, while the small particles may provide most of the perpendicularly polarized radiation. White particles have spent their energy budget in scattering and have little left over for thermal emission. Black particles, on the other hand, absorb sunlight to emit their own spectrum almost isotropically in the infrared. Particles close to the Sun intercept more energy and therefore have a larger budget. We should therefore not expect that the same average dust properties will fit both optical and infrared data, or optical data at different elongation angles from the Sun. Besides these optical biases there are also orbital dynamic biases. Particles experiencing a given drag in low inclination orbits accommodate better to the local precession plane than similar particles in high inclination, slowly precessing orbits. Their symmetry planes therefore are different as is seen in the *IRAS* data (Dermott et al 1992). It is therefore no

surprise that the zodiacal dust cloud has the appearance of a heterogeneous mixture of dust with average optical and thermal properties that depend on the position in the solar system. If we learn to use these biases to our advantage, this might allow us to selectively study components of known origin and of some known particle characteristics.

There is evidence of real differences between dust populations other than what can be expected from bias (Levasseur-Regoud et al 1991, Hanner 1991). The challenge is to identify components of the dust cloud and thereby enable the study of interplanetary dust to be put in a proper context. The contribution from six Hirayama families has been identified by Dermott et al (1993b) and separated from the background. Their contribution is $\sim$10% of the total brightness at 25 μm and the total contribution from the main asteroid belt is estimated to be 1/3 of the total and could be larger. Short period comets are seen to eject material into interplanetary space but a large amount of the visible dust immediately leaves the solar system. Radiation pressure elevates dust particles' potential energy over that of the parent body and the total energy (kinetic plus potential) often leads to unbound trajectories. This is particularly common for release near perihelion where dust production normally peaks. However, many meteor streams are associated with comets and as meteoroids gradually grind down, dust-size comet matter may have a larger chance of reaching a bound orbit.

Recent advances in modeling capabilities and comparisons with observations have led to the realization of new methods to distinguish dust based on its origin and average dynamic drag. This may be the breakthrough that will finally allow us to answer the age-old question of the origin and evolution of the interplanetary dust cloud. The issue has been hotly debated at least since the time of the First World War when Fesenkov (1914) suggested that disintegrating periodic comets feed the interplanetary dust cloud. It is my hope that this review of the physics on which the dynamic modeling of the zodiacal dust cloud depends, and of the optical and thermal dust properties that affect the bias, will contribute to this progress.

ACKNOWLEDGMENTS

I am grateful to my family, friends, and colleagues, who each in some way influenced or inspired my work. I am particularly indebted to Prof. S. F. Dermott (Univ. of Florida, USA), the late Prof. R. H. Giese (Ruhr Univ., FRG), Prof. J. M. Greenberg (Univ. Leiden, Netherlands), and Prof. E. Grün (Max-Planck-Institut für Kernphysik, FRG). Graduate students L. G. Adolfsson, D. D. Durda, S. Jayaraman, and J. C. Liou reviewed

the manuscript. This work was supported by NASA through grants No. NAGW-2775 and NAGW-2482.

Literature Cited

Alfvén H. 1977. Electric currents in cosmic plasmas. *Rev. Geophys. Space Phys.* 15(3): 271–84

Antyukh EV, Braginskii VB, Manukin AB. 1973. Astrophysical consequences of pondermotive effects of electromagnetic radiation. *Sov. Astron. AJ* 16(5): 893–95

Ashworth DG. 1978. Lunar and planetary impact erosion. In *Cosmic Dust*, ed. JAM McDonnell, pp. 427–526. Chichester: Wiley

Binzel RP, Gehrels T, Matthews MS, eds. 1989. *Asteroids II*. Tucson: Univ. Ariz. Press

Bradley JP. 1991. Newly developed techniques for the analysis of micrometer-sized interplanetary dust particles and comet grains. *Space Sci. Rev.* 56: 131–38

Bruggeman DAG. 1935. Berechnung verschiedener physikalischer Konstanten von heterogenen Substanzen 1. Dielektrizitätskonstanten und Leitfähigkeiten der Mischkörper aus isotropen Substanzen. *Ann. Phys. (Leipzig)* 24: 636–79

Bruno R, Villante U, Bavassano B, Schwenn R, Mariani F. 1986. In-situ observations of the latitudinal gradients of the solar wind parameters during 1976 and 1977. *Sol. Phys.* 104: 431–45

Burns JA, Lamy PL, Soter S. 1979. Radiation forces on small particles in the solar system. *Icarus* 40: 1–48

Chapman CR, Paolicchi P, Zappal V, Binzel RP, Bell JF. 1989. Asteroid families: Physical properties and evolution. See Binzel et al 1989, pp. 386–415

Dermott SF, Durda DD, Gustafson BÅS, Jayaraman S, Xu YL, et al. 1993b. *Proc. IAU Symp.* 160 In press

Dermott SF, Durda DD, Gomes RS, Gustafson BÅS, Jayaraman S, et al. 1993a. Origin of the IRAS dustbands. In *Meteoroids and their Parent Bodies*, ed. J Štohl, IP Williams, pp. 357–66. Bratislava: Astron. Inst., Slovak Acad. Sci.

Dermott SF, Gomes RS, Durda DD, Gustafson BÅS, Jayaraman S, et al. 1992. Dynamics of the Zodiacal cloud. In *Chaos, Resonance, and Collective Dynamical Phenomena in the Solar System*, ed. S Ferraz-Mello, pp. 333–47. Dordrecht: Kluwer

Dermott SF, Jayaraman S, Xu YL, Liou JC. 1993c. *IRAS* observations show that the Earth is embedded in a solar ring of asteroidal dust particles in resonant lock with the planet. *Bull. Am. Astron. Assoc.* 25(3): 1116

Dermott SF, Nicholson PD, Burns JA, Houck JR. 1984. Origin of the Solar System dust bands discovered by IRAS. *Nature* 312: 505–9

Dohnanyi JS. 1978. Particle dynamics. In *Cosmic Dust*, ed. JAM McDonnell, pp. 527–605. Chichester: Wiley

Draine BT, Lee HM. 1984. Optical properties of interstellar graphite and silicate grains. *Astrophys. J.* 285: 89–108

Durda DD, Dermott SF, Gustafson BÅS. 1992. Modeling of asteroidal dust production rates. In *Asteroids, Comets, Meteors* 1991, ed. AW Harris, ELG Bowell, pp. 161–64. Houston: Lunar Planet. Inst.

Fessenkov VG. 1914. Sur l'origine de la lumière zodiacale. *Astron. Nachr.* 198(4752): 465–71

Flynn GJ, Sutton SR. 1990. Evidence for a bimodal distribution of cosmic dust densities. *Proc. Lunar Sci. Conf. XXI*, pp. 375–76

Fujiwara A. 1987. Energy partition into translational and rotational motion of fragments in catastrophic disruption by impact: an experiment and asteroid cases. *Icarus* 70: 536–45

Fujiwara A, Cerroni P, Davis D, Ryan E, Di Martino M, et al. 1989. Experiments and scaling laws for catastrophic collisions. See Binzel et al 1989, pp. 240–65

Giese RH. 1973. Optical properties of single-component zodiacal light models. *Planet. Space Sci.* 21: 513–21

Giese RH, Kneissel B, Rittich U. 1986. Three-dimensional zodiacal dust cloud: a comparative study. *Icarus* 68: 395–411

Goertz CK. 1989. Dusty plasmas in the solar system. *Rev. Geophys.* 27: 271–92

Gold T. 1952. The alignment of galactic dust: *Mon. Not. R Astron. Soc.* 112: 215–18
Gradie JC, Chapman CR, Tedesco EF. 1989. Distribution of taxonomic classes and the compositional structure of the asteroid belt. See Binzel et al 1989, pp. 316–35
Greenberg JM. 1988. The interstellar dust model of comets: post Halley. In *Dust in the Universe*, ed. M Bailey, DA Williams, pp. 121–43. Cambridge: Cambridge Univ. Press
Greenberg JM, Gustafson BÅS. 1981. A comet fragment model for Zodiacal light particles. *Astron. Astrophys.* 93: 35–42
Greenberg JM, Hage JI. 1990. From interstellar dust to comets: a unification of observational constraints. *Astrophys. J.* 361: 260–74
Grün E, Gustafson BÅS, Mann I, Baguhl M, Morfill GE, et al 1993b. Interstellar dust in the heliosphere. *Astron. Astrophys.* Submitted
Grün E, Zook HA, Baguhl M, Balogh A, Bame SJ, et al. 1993. Discovery of Jovian dust streams and interstellar grains by the *Ulysses* spacecraft. *Nature* 362: 428–30
Grün E, Zook HA, Fechtig H, Giese RH. 1985. Collisional balance of the meteoritic complex. *Icarus* 62: 244–72
Gustafson BÅS. 1989. Comet ejection and dynamics of nonspherical dust particles and meteoroids. *Astrophys. J.* 337: 945–49
Gustafson BÅS, Misconi NY. 1979. Streaming of interstellar grains in the solar system. *Nature* 282: 276–78
Gustafson BÅS, Misconi NY. 1986. Interplanetary dust dynamics I. Long-term gravitational effects of the inner planets on zodiacal dust. *Icarus* 66: 280–87
Gustafson BÅS, Misconi NY, Rusk ET. 1987. Interplanetary dust dynamics III. Dust released from P/Encke: distribution with respect to the zodiacal cloud. *Icarus* 72: 582–92
Gustafson BÅS, Grün E, Dermott SF, Durda DD. 1992. Collisional and dynamic evolution of dust from the asteroid belt. In *Asteroids, Comets, Meteors* 1991, ed. AW Harris, ELG Bowell, pp. 223–26. Houston: Lunar Planet. Inst.
Hage JI, Greenberg JM. 1990. A model for the optical properties of porous grains. *Astrophys. J.* 361: 251–59
Hanner MS. 1981. On the detectability of icy grains in the comae of comets. *Icarus* 47: 342–50
Hanner MS. 1991. The infrared zodiacal light. In *Origin and Evolution of Interplanetary Dust*, ed. AC Levasseur-Regourd, H Hasegawa, pp. 171–78. Tokyo: Kluwer
Jones W. 1990. Rotational damping of small interplanetary particles. *Mon. Not. R. Astron. Soc.* 247: 257–59
Klačka J. 1992. Poynting-Robertson effect I. Equation of motion. *Earth, Moon and Planets* 59: 41–59
Kojima M, Kakinuma T. 1990. Solar cycle dependence of global distribution of solar wind speed. *Space Sci. Rev.* 53: 173–222
Krueger FR, Korth A, Kissel J. 1991. The organic matter of comet Halley as inferred by joint gas phase and solid phase analyses. *Space Sci. Rev.* 56: 167–75
Lamy PL, Perrin JM. 1991. The optical properties of interplanetary dust. In *Origin and Evolution of Interplanetary Dust*, ed. AC. Levasseur-Regourd, H. Hasegawa, pp. 163–70. Tokyo: Kluwer
Lichtenegger HIM, Kömle NI. 1991. Heating and evaporation of icy particles in the vicinity of comets. *Icarus* 90: 319–25
Leinert C, Grün E. 1990. Interplanetary dust. In *Physics of the Inner Heliosphere I*, ed. R Schwenn, E Marsch, 207–75. Heidelberg: Springer-Verlag
Levasseur-Regourd AC, Renard JB, Dumont R. 1991. The zodiacal cloud complex. In *Origin and Evolution of Interplanetary Dust*, ed. AC Levasseur-Regourd, H Hasegawa, pp. 131–38. Tokyo: Kluwer
Lipschutz ME, Gaffey MJ, Pellas P. 1989. Meteoritic parent bodies: nature, number, size and relation to present-day asteroids. See Binzel et al 1989, pp. 740–77
Love SG, Brownlee DE. 1991. Heating and thermal transformation of micrometeoroids entering the Earth's atmosphere. *Icarus* 89: 26–43
Mariani F, Neubauer FM. 1990. The interplanetary magnetic field. In *Physics of the Inner Heliosphere I*, ed. R Schwenn, E Marsch, pp. 183–206. Heidelberg: Springer-Verlag
Marsden BG, 1976. Nongravitational forces on comets. In *The Study of Comets*, ed. B Donn, M Jackson, M A'Hearn, R Harrington, pp. 465–89. *NASA SP*-393
Maxwell Garnett JC. 1904. Colors in metal glasses and in metallic films. *Phil. Trans. R. Soc.* A203: 385–420
Moulton FR. 1970. *An Introduction to Celestial Mechanics*. New York: Dover
Mukai T, Yamamoto T. 1982. Solar wind pressure on interplanetary dust. *Astron. Astrophys.* 107: 97–100
Paddack SJ, Rhee JW. 1976. Rotational bursting of interplanetary dust particles. In *Interplanetary Dust and Zodiacal Light*, ed. H Elsässer, H. Fechtig, pp. 453–57. Berlin: Springer-Verlag
Parker EN. 1958. Dynamics of the interplanetary gas and magnetic fields. *Astrophys. J.* 128: 664–75
Patashnik H, Rupprecht G. 1975. The life-

time of ice particles in the solar system. *Icarus* 30: 402–12
Purcell EM, Pennypacker CR. 1973. Scattering and absorption of light by nonspherical dielectric grains. *Astrophys. J.* 186: 705–14
Radzievskii VV. 1952. On the influence of an anisotropic re-emission of solar radiation on the orbital motion of asteroids and meteorites. *Astron. Zh.* 29: 162–70. US Dept. Commerce Transl. 62–10653
Rickman H. 1989. The nucleus of comet Halley: surface structure, mean density, gas and dust production. *Adv. Space Res.* 9(3): 59–71
Rickman H, Fernández JA, Gustafson BÅS. 1990. Formation of stable dust mantles on short-period comet nuclei. *Astron. Astrophys.* 237(2): 524–35
Rickman H, Kamél L, Froeschlé C, Festou MC. 1991. Nongravitational effects and the aging of periodic comets. *Astron. J.* 102(4): 1446–63
Sagdeev RZ, Elyasberg PE, Moroz VI. 1988. Is the nucleus of comet Halley a low density body? *Nature* 331: 240
Saito T. 1988. Solar cycle variation of solar, interplanetary, and terrestrial phenomena. In *Laboratory and Space Plasmas*, ed. H Kikuchi, pp. 473–528. New York: Springer-Verlag
Sanford SA, Walker RM. 1985. Laboratory infrared transmission spectra of individual interplanetary dust particles from 2.5 to 25 microns. *Astrophys. J.* 291: 838–51
Schwenn R. 1990. Large-scale structure of the interplanetary medium. In *Physics of the Inner Heliosphere I*, ed. R Schwenn, E Marsch, pp. 99–181. Heidelberg: Springer-Verlag
Seab CG. 1987. Grain destruction, formation, and evolution. In *Interstellar Processes*, ed. DJ Hollenbach, HA Thronson Jr, pp. 491–512. Dordrecht: Reidel
Shul'man LM. 1972. The evolution of cometary nuclei. In *The Motion, Evolution of Orbits, and Origin of Comets*, ed. GA Chebotarev, EI Kazimirchak-Polonskaya, BG Marsden, pp. 271–76. Dordrecht: Reidel
Smith EJ, Tsurutani BT, Rosenberg LR. 1978. Observations of the interplanetary sector structure up to heliographic latitudes of 16, Pioneer 11. *J. Geophys. Res.* 83: 717–24
Standish EM Jr, Hellings RW. 1989. A determination of the masses of Ceres, Pallas, and Vesta from their perturbations upon the orbit of Mars. *Icarus* 80: 326–33
Steinitz R, Eyni M. 1980. Global properties of the solar wind. I The invarience of the momentum flux density. *Astrophys. J.* 241: 417–24
Suess HE. 1987. *Chemistry of the Solar System*. New York: Wiley
Thiel K, Bradley JP, Spohr R. 1991. Investigation of solar flare tracks in IDPs: some recent results. *Nucl. Tracks Rad. Measurements* 19: 709–16
van de Hulst HC. 1957. *Light Scattering by Small Particles*. New York: Wiley
Weber EJ, Davis L. 1967. The angular momentum of the solar wind. *Astrophys. J.* 148: 217–27
Weidenschilling SJ. 1981. How fast can an asteroid spin? *Icarus* 46: 124–26
Weinberg JL. 1985. Zodiacal light and interplanetary dust. In *Properties and Interactions of Interplanetary Dust*, ed. RH Giese, P Lamy, pp. 1–6. Dordrecht: Reidel
Weinberg JL, Sparrow JG. 1978. Zodiacal light as an indicator of interplanetary dust. In *Cosmic Dust*, ed. JAM McDonnell, pp. 75–122. Chichester: Wiley
Wetherill GW. 1985. Asteroidal source of ordinary chondrites. *Meteoritics* 20: 1–22
Xu YL, Dermott SF, Durda DD, Gustafson BÅS, Jayaraman S, Liou JC. 1993. The Zodiacal Cloud. In *The Ceremony of the 70th Anniversary of the Chinese Astronomical Society*. Beijing: Chinese Acad. Sci. In press
Zerull RH, Gustafson BÅS, Schulz K, Thiele-Corbach E. 1993. Scattering by aggregates with and without an absorbing mantle; microwave analog experiments. *Appl. Opt.* 32(21): 4088–100